Influence of Crystallographic Orientation in Normal and Sliding Contacts

A thesis
Presented to
The academic faculty

By

Jeremy J. Dawkins

In Partial Fulfillment
Of the Requirements for the Degree
Master of Science in Mechanical Engineering

Georgia Institute of Technology

August 2008

Influence of Crystallographic Orientation in Normal and Sliding Contacts

Approved By:

Dr. Richard Neu, Advisor
G.W. W. School of Mechanical Engineering
Georgia Institute of Technology

Dr. Itzhak Green
G.W. W. School of Mechanical Engineering
Georgia Institute of Technology

Dr. Jeffrey Streator
G.W. W. School of Mechanical Engineering
Georgia Institute of Technology

Date Approved: April 30, 2008

To my grandparents:
James F. Dawkins Sr. & Virginia F. Dawkins
Jesse A. Hobbs Sr. & Mabel W. Hobbs

ACKNOWLEDGEMENTS

First, I would like to give glory and honor to God for giving me the mental and physical strength as well as the opportunity to conduct this work towards completing my master's degree. I would like to thank my fiancée Shaneé Wright, my Parents James and Alice Dawkins, my Siblings Jamil and Kenia Smith, Darren Dawkins, and the rest of my family for their continued love and support during my studies.

I would also like to thank my Advisor Dr. Richard W. Neu, for his mentorship and guidance during my studies. The help of my colleagues in the Mechanics of Materials group is also greatly appreciated. This work was supported by the National Science Foundation under Grant No. CMS-0510209.

TABLE OF CONTENTS

LIST OF TABLES

LIST OF FIGURES

SUMMARY

The aim of this study is to evaluate a methodology for modeling the influence of crystallographic grain orientation on key parameters in normal and sliding contacts. The simulations of interfering cylindrical asperities, using finite element analysis, were conducted using two different plasticity models for copper: a conventional isotropic, homogeneous J_2 plasticity model and a continuum crystal plasticity model. A normal contact study was conducted in which crystallographic orientation effects on different parameters were investigated. The model was then adapted for sliding contacts, which allowed other parameters such as energy dissipation to be investigated. Using crystal plasticity, the dependence of crystallographic orientation on plastic deformation and energy dissipation can be determined. The relative trends predicted using crystal plasticity are consistent with experiments that show friction depends on crystallographic orientation when plastic deformation is one of the primary energy dissipation mechanisms.

CHAPTER 1: INTRODUCTION

Friction and wear create problems at some level in virtually every industry; this problem is ultimately one of interacting surfaces. Accurately modeling surface interactions is the first step in designing surfaces which are resistant to various types of wear or with desirable frictional properties. One of the elements of this broader goal to accurately model surface interactions is to model microstructural effects on contacting surfaces. The purpose of this study is to develop methods to capture microstructural features in contact mechanics. This will lead to an increased understanding of the important modeling considerations that must be taken to accurately model more complex contact problems. Specifically the influence of crystallographic orientation on stresses, strains, and forces in normal and sliding contacts will be modeled. The sizing and spacing of contacting asperities at a certain scale are on the same length scale as key microstructural attributes such as grain size and orientation, yet these attributes are rarely captured in contact mechanics models. Investigating the influence of these features can give us a more physically realistic understanding of microstructure in contact mechanics.

Past work considering normal interference [1-5] or sliding interference between two bodies [6-8] do not explicitly consider these microstructural attributes, treating the material as initially isotropic and homogeneous. One could consider molecular dynamics simulations [9-11]. However, the size and spacing of asperities are usually much larger in scale in typical sliding contact applications than that which can be modeled efficiently using molecular dynamics. It is also desirable to have an approach to bridge the length-scale gap between molecular dynamic simulations and the continuum homogeneous macroscale simulations.

Success has recently been gained in understanding the relationship between different microstructure attributes and the local response that controls the fretting fatigue behavior by using a crystal plasticity material model [12-14]. In this study the aim is to determine whether continuum crystal plasticity can also predict similar variations in stress, strain, and coefficient of friction (COF) with crystallographic orientation in sliding contacts.

Experiments have shown that the COF depends on crystallographic orientation. When sliding on the cubic face (001) of single crystal FCC Cu, the COF is two to three times greater in the ⟨110⟩ direction compared to the ⟨100⟩ direction as shown in Figure 1 [15]. The experiments were conducted sliding a stationary stylus on a rotating single crystal Cu disk in an inert atmosphere. As the disk rotated, the direction of sliding relative to the crystal orientation changed in a sinusoidal manner. Here, the load is quite high, $P/P_y > 600$, where P is the normal force and P_y is the normal force at the onset of yielding of the initially annealed Cu assuming macroscopic isotropic behavior. A later study [16] of sliding on the cubic face of Cu with $P/P_y > 10^4$ verified these trends and further focused on the deformation substructures that formed as a result of the sliding. The greatest COF, 1.25, was also in the ⟨110⟩ direction and lowest COF, 0.9, in the ⟨100⟩ direction, while sliding along the intermediate ⟨210⟩ direction resulted in a COF of 1.0. The degree of plastic deformation, which is inversely proportional to the cell size under the groove of the friction track, scaled the same way, ⟨110⟩ > ⟨210⟩ > ⟨100⟩. The higher COFs were obtained when multiple slip systems were activated. The lowest COF occurred when single slip took place. Generally, the COF is lower on planes of high atomic density, which can also be sheared via single slip [17].

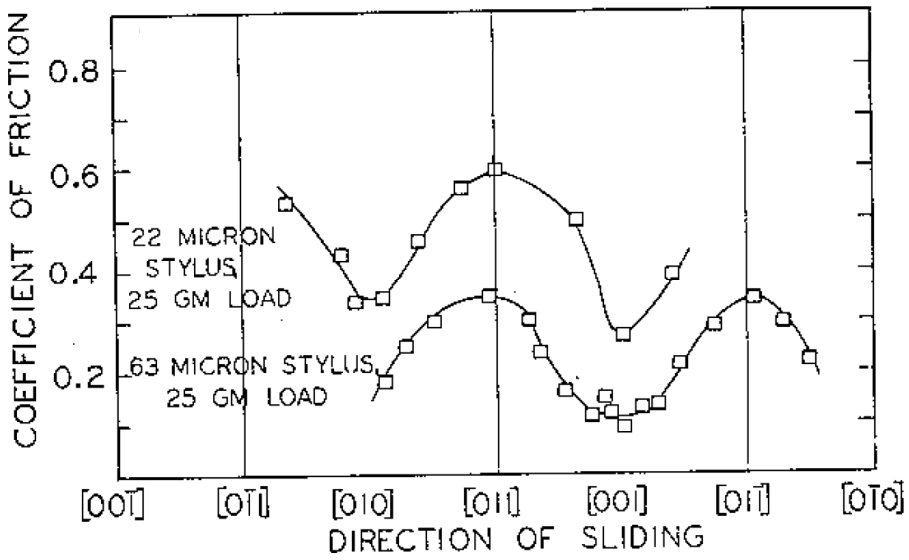

(a)

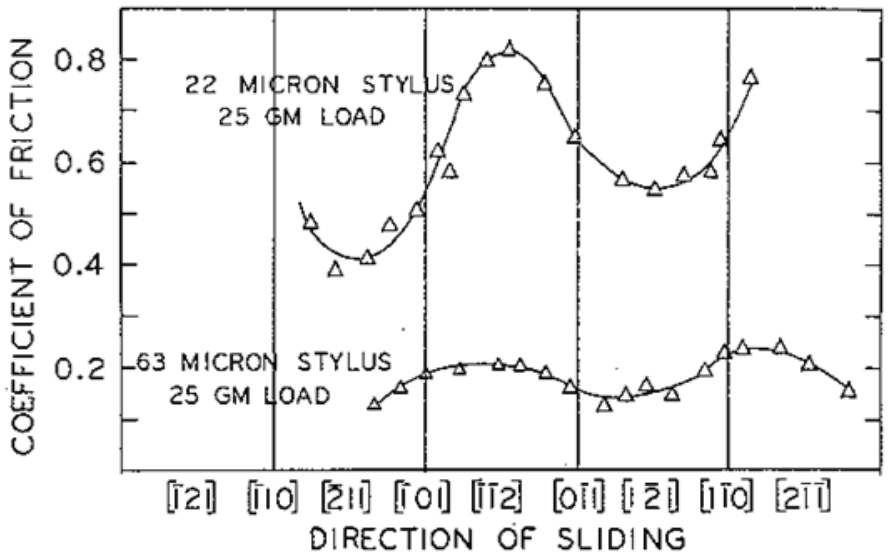

(b)

Figure 1: Friction measurements on single crystal of copper on the (a) (001) face (b) (111) face [15].

The surface roughness in a turning process on a single crystal of copper has also been related to the orientation of the crystal. Lee et al. [18] showed that when turning a (001) face of a single crystal of copper the roughness in the equivalent ⟨100⟩ directions is

lower than in the other directions shown in Figure 2. They also observed patterns in the directions of the roughness on other planes as well. The decreased roughness is explained in part by the increased elastic recovery in this direction, though certainly the anisotropy of the plastic deformation plays a large role too.

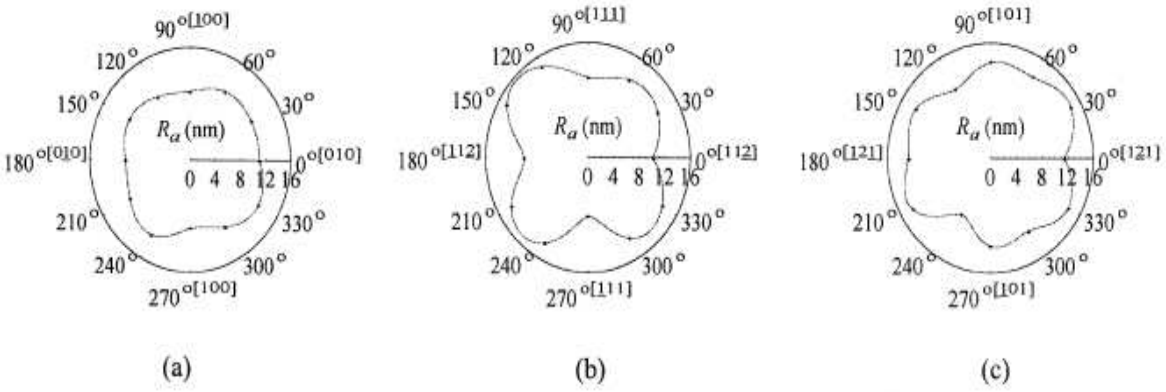

Figure 2: Variation of surface roughness for diamond turning of copper single crystals when the cutting plane is (a) (001) plane (b) (110) plane, and (c) (111) plane [18].

One of the first models to explicitly relate COF to the crystallographic orientation and resistance to plastic deformation is that of Kuhlmann-Wilsdorf [19],

$$COF = C\left(\frac{\tau_s}{\tau_b}\right)\left(\frac{m_b}{m_s}\right) \tag{1}$$

where τ_s and τ_b are the crystallographic shear strengths of the work-hardened surface and bulk material, respectively, and m_s and m_b are the Schmid factors for the surface and bulk material, respectively; C is a constant associated with contact area. This model implies that when the surfaces of the two bodies are oriented for easy shear, the COF decreases.

When indenting a single crystal of copper on the (001) cube face with a sphere the shape that results is nearly square [20], shown in Figure 3. The reason for this is both the

elastic and plastic anisotropies. During the penetration of the indenter, more plastic deformation occurs in the ⟨110⟩ directions than in the ⟨100⟩ directions. This is caused partially because the elastic modulus in the ⟨110⟩ is much higher and thus the resolved shear stress in these directions increases more rapidly reaching the yield surface sooner and the higher stress causes more slip systems to be activated. This is combined with more elastic recovery in the ⟨100⟩ resulting in the observed shape. Similar trends have been observed indenting a single crystal Ni-base superalloy [21].

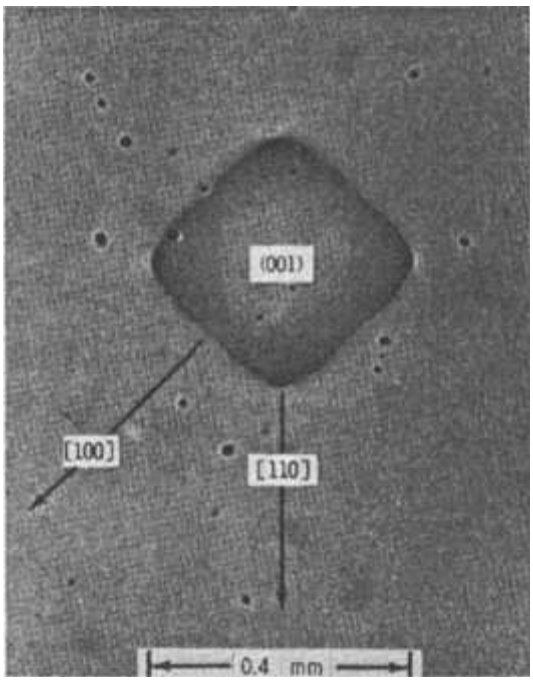

Figure 3: Indentation of single crystal Cu on (001) plane with 6.35 mm ball and 10 N force [20].

Within the past few years there has been work done studying normal contacts from different perspectives. Jackson and Green [1], and Kogut and Etison [4], conducted finite element studies investigating the loaded response of contact of a sphere on a flat. Mesarovic and Fleck [5] performed a finite element study to understand the behavior of elastic-plastic dissimilar spheres. Later Jackson and Green [2] extended their previous

work to investigate the residual stress formations for a sphere on flat. Although these works were all 3D analyses, they used elastic-plastic material models which cannot capture the anisotropies which are present in a single crystal. More recently, Casals et al. [22] has performed work modeling Vickers and Berkovich hardness tests on single crystals of copper using 3D finite element analysis with crystal plasticity. They found that crystal plasticity is an effective tool for capturing the response of indenting single crystals.

Since asperities deform plastically during sliding contact, friction can be addressed in a fundamental sense by studying interacting asperities. If no COF is imposed at the contact, all the work done translating the cylinders is associated with plastic dissipation, determined by summing the horizontal reaction forces over the distance in which the asperities interact. Recently Vijaywargiya and Green [8] studied 2D interfering asperities using an elastic-plastic finite element model. Two cylindrical asperities are initially offset and an interference ω is prescribed between them. Using displacement boundary conditions, the top cylinder is translated bringing the cylinders into contact and then back out of contact as illustrated in Figure 4. The von Mises stress for a normalized interference (ω^*) of 20 is shown in Figure 5. The surfaces are prescribed as frictionless to isolate plastic deformation as the source for energy dissipation. The total energy dissipation for sliding one asperity by the other is quantified by taking the summation of the horizontal reaction forces over the distance that the top cylinder traversed,

$$U_{net} = \int_{x_1}^{x_2} F_x dx \tag{2}$$

where U_{net} is the total work done and F_x is the net horizontal reaction force at the base nodes of the bottom cylinder. As U_{net} increases the measured COF will also increase.

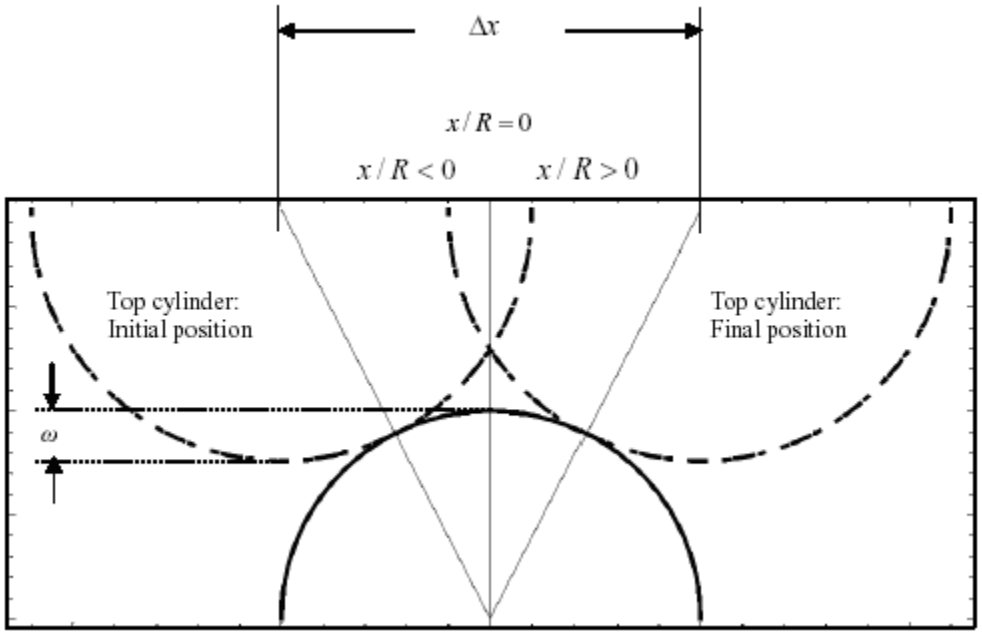

Figure 4: Schematic of the sliding process.

By increasing the prescribed interference ω, the deformation at the contact interface increases. The energy dissipation exhibits a 2nd order polynomial dependence on interference shown in Figure 6 [8]. In addition, more energy is invested sliding one cylinder across the other than that is returned when the cylinders are repelling each other. During sliding the maximum contact width occurs prior to the axes of the two cylinders being aligned.

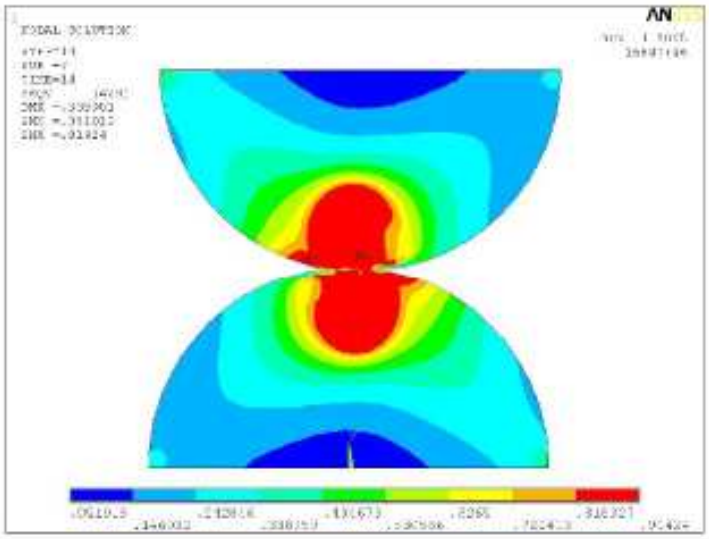

Figure 5 : von Mises stress at maximum interference for ω*=20 [8].

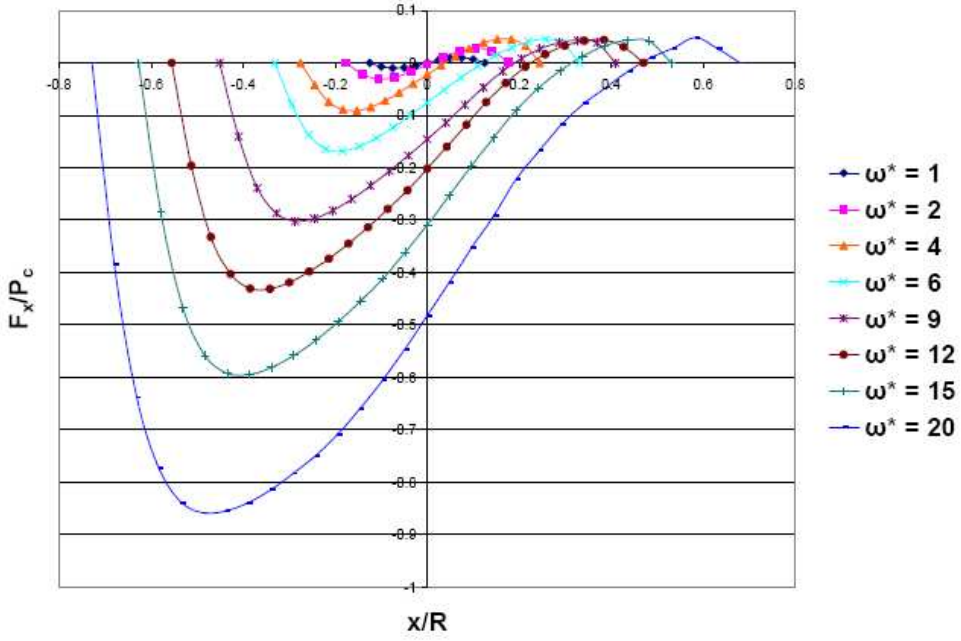

Figure 6: Normalized horizontal reaction force vs. normalized sliding distance [8].

This work will study both normal and sliding contacts. The same FE model and mesh will be used and the boundary conditions and load steps will be altered to suit the normal and sliding contact simulations. Continuum crystal plasticity is used to capture the anisotropic elastic-plastic behavior of single crystal Cu. The crystal plasticity model allows us to prescribe the crystallographic orientation of one or both of the asperities. The effects of these orientations are then compared to determine their relative influence on the response. By first studying the more simple case of normal contacts, we will have a more complete understanding of the more complex sliding case. Any material dependence on plastic dissipation can be investigated with these simulations. In the sliding contact simulations these comparisons can also be extended to energy dissipation and hence their influence on the COF.

CHAPTER 2: MATERIAL MODELS

2.1 Formulation

Two plasticity models were used in this investigation. The first is a conventional J_2 elastic-plastic model with isotropic hardening and the second a continuum crystal plasticity model. For the conventional model, the plastic material definition in ABAQUS [23] was used. The stress-plastic strain response for oxygen-free high-conductivity (OFHC) copper is shown in Figure 7 [24]. The elastic-plastic J_2 model requires defining both the elastic properties of the material as well as effective stress-plastic strain data to describe the plastic flow and hardening behavior [24]. For the conventional model, the experimental data points were input as the referenced response with initial yield strength of 37 MPa. The elastic properties used in the conventional isotropic model are E = 140 GPa and $\nu = 0.33$.

The crystal plasticity model is implemented as a user-defined material (UMAT) subroutine for ABAQUS [23]. The crystal plasticity model for Cu was developed by McGinty and McDowell [25]. Face centered cubic (FCC) Cu has 12 systems of the type $(111)\langle 01\bar{1}\rangle$ and this material model accounts for these slip systems. To specify the crystallographic orientation, the Euler angles are prescribed at each integration point. The crystal plasticity model takes into account isotropic hardening and it also has terms to deal with kinematic hardening but for these simulations of Cu, those terms were not necessary and hence set to zero. The framework for the model is rate dependent but the high stress exponent in the flow rule causes it to behave as a nearly rate-independent model. In the original development of the crystal plasticity model [25], the large strain

response was studied, and hence the elastic behavior was insignificant and isotropic elastic properties were used. However, in this study since the elastic and plastic deformation are both similar in magnitude, the anisotropic elastic constants for Cu need to be used: C_{11}=168.4GPa, C_{12}=121.4GPa, C_{44}=75.5GPa [26].

The details of the crystal plasticity model and its implementation are found in McGinty and McDowell [25]. Some specifics related to modeling Cu are noted here. The flow rule, which relates the strain rate $\dot{\gamma}^{(\alpha)}$ on slip system α to the resolved shear stress on that system is given by

$$\dot{\gamma}^{(\alpha)} = 0.001\left|\frac{\tau^{(\alpha)} - \chi^{(\alpha)}}{g^{(\alpha)}}\right|^{\frac{1}{0.02}} \mathrm{sgn}(\tau^{(\alpha)} - \chi^{(\alpha)}) \tag{3}$$

where $\tau^{(\alpha)}$ is the resolved shear stress on slip system α, $\chi^{(\alpha)}$ is the back stress, which is an internal state variable that describes the kinematic hardening effect on slip system α, and $g^{(\alpha)}$ is the drag strength, which is an internal state variable associated with the yield strength on slip system α. For Cu, the back stress was set to zero and did not evolve and the drag strength $g^{(\alpha)}$ was initially set to 13 MPa. The evolution of the drag strength, which controls isotropic hardening, is given by

$$\dot{g}^{(\alpha)} = 225\sum_{\beta=1}^{N_{sys}}\left|\dot{\gamma}^{\beta}\right| - 2.05g^{(\alpha)}\sum_{\beta=1}^{N_{sys}}\left|\dot{\gamma}^{\beta}\right| \tag{4}$$

2.2 Validation

The model constants including the coefficients and exponents in Eqs. (3) and (4) were first calibrated by McGinty and McDowell [25] using a generalized Taylor model with 300 randomly-oriented grains. The constants were determined by trial and error until

the macroscopic model response matched that of the polycrystal Cu response as shown in Figure 7. Later the calibration was verified by simulating a volume element with periodic boundary conditions under a uniaxial load that contained 64 randomly-orientated crystals. The internal stresses at the end of the loading is shown in Figure 8. The corresponding predicted macroscopic response is shown in Figure 7. The grains are represented by a grouping of 2 x 2 x 2 elements. Clearly each grain undergoes a different response in the polycrystalline model because of the interactions among the grains as a result of the different deformations within each grain. Note that the stresses locally are as high as 429 MPa when the maximum aggregate response is only 330 MPa. This demonstrates the local response variations.

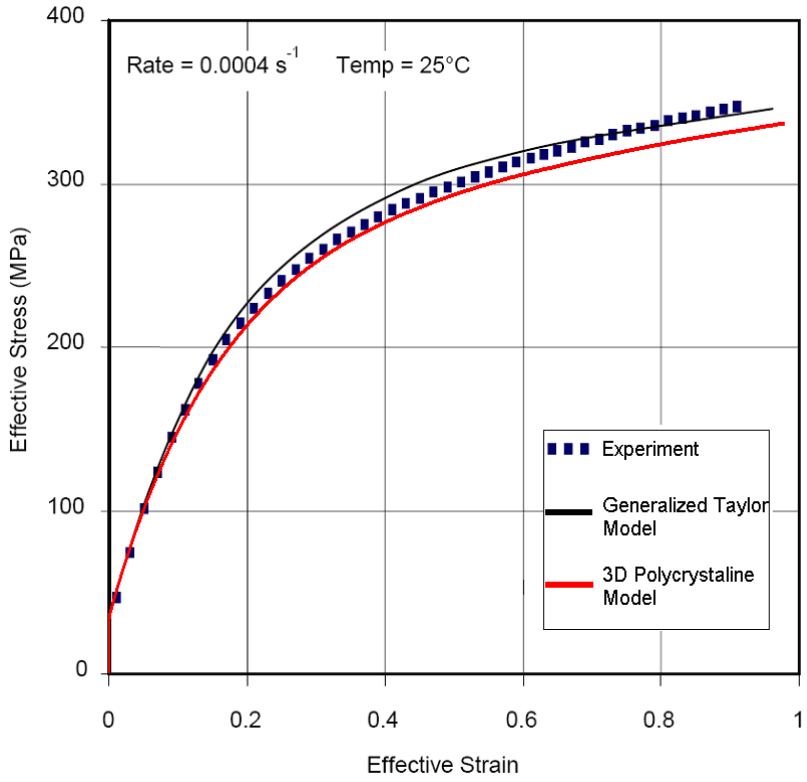

Figure 7: Stress strain data used to validate crystal plasticity model.

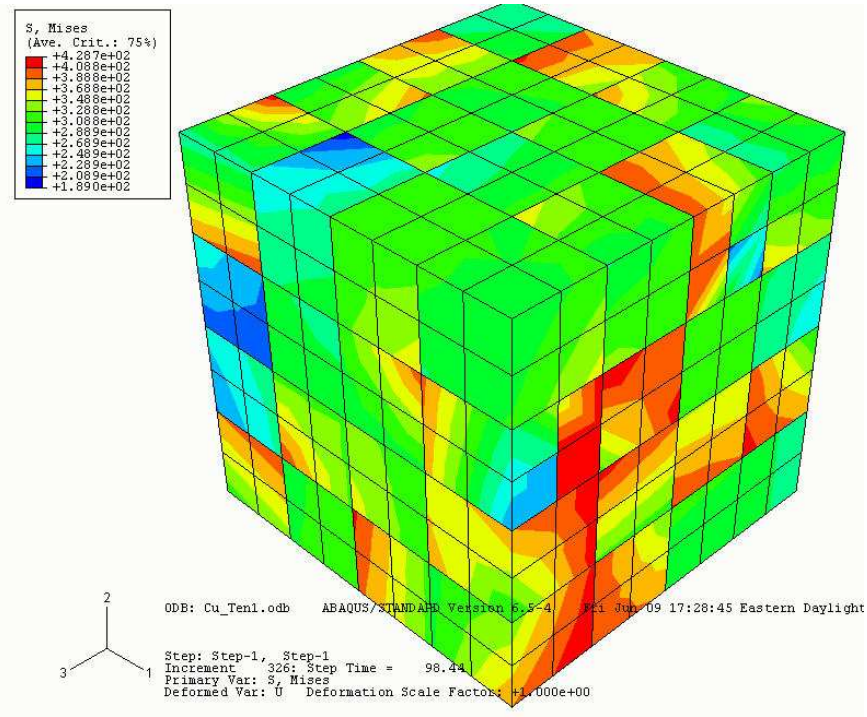

Figure 8: Polycrystalline representative volume element loaded in tension.

2.3 Orientations

One of the key objectives of this study is to develop a model which can be used to capture some of the orientation effects which have been observed experimentally [15, 17, 20] for a single crystal of copper. To determine which simulations to run to best understand the trends of orientation effect of plastic deformation, we can use the COF results reported by Bailey and Gwathmey [15]. The orientations for all of the simulations run are shown in Figure 9, the red lines outline the plane on which the interface direction was set, and the dotted lines show the sliding direction. The interface plane and sliding direction are shown relative to the cylinders in Figure 10. When sliding on a {001} plane the maximum coefficient of friction was measured in the ⟨110⟩ directions with a minimum occurring in the ⟨100⟩ directions. When sliding on a {110} plane the results for

the maximum and minimum directions were not reported, so to determine them the three directions shown in Figure 9(b) were chosen. It is hypothesized that the two extreme directions will be in the ⟨100⟩ and the $\langle \bar{1}10 \rangle$, with one being the minimum COF and one being the maximum COF and the COF in the $\langle \bar{1}11 \rangle$ direction will fall somewhere between. The (111) plane typically has trisymmetry, with the minimum COF occurring in the $\langle \bar{2}11 \rangle$ directions and the maximum COF occurring in the $\langle 2\bar{1}\bar{1} \rangle$ directions [15]. This effectively represents sliding in to opposite directions, towards the point or towards the base of the triangle the (111) plane creates in the unit cube. In an FCC crystal the slip occurs in the directions $\langle 01\bar{1} \rangle$. It can be seen from Figure 9(c) that the interaction of dislocations along the slip direction will be different, interfering in one direction but not in the other.

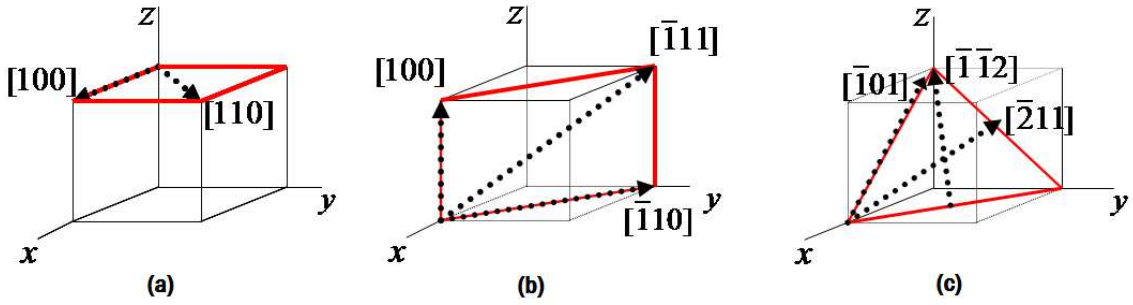

Figure 9: Simulation sliding directions for (a) (001) (b) (110) (c) (111).

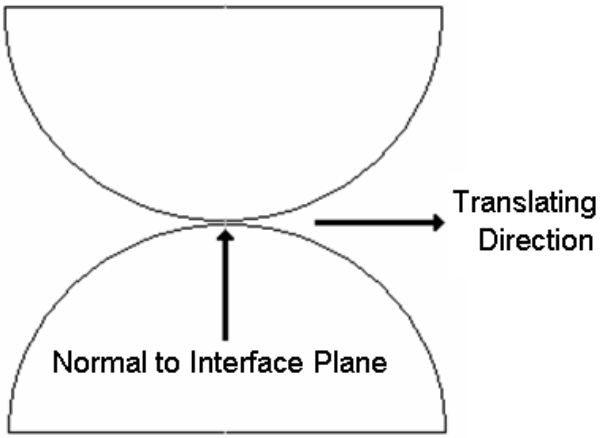

Figure 10: Interface plane and translating direction shown relative to the position on the cylinders.

There are several conventions for the definitions of Euler angles, one of the most common [27] and the one used in this study is the Bunge convention. According to the Bunge convention φ_1 is a rotation about the global z axis, ϕ is a rotation about the new local x axis, and φ_2 is a rotation about the new local z axis as shown in Figure 11 .

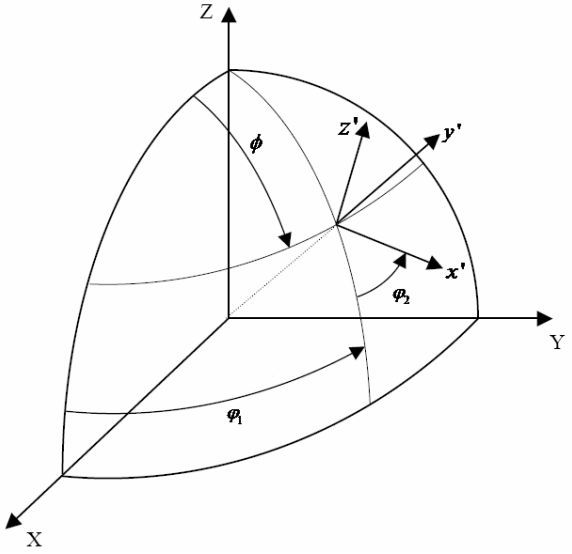

Figure 11: Bunge convention of describing crystal orientation by rotations about, global z-axis, local x-axis, and local z-axis.

The matrix for these three rotations is written

$$a_{ij} = \begin{bmatrix} b_1 & t_1 & n_1 \\ b_2 & t_2 & n_2 \\ b_3 & t_3 & n_3 \end{bmatrix} = \begin{bmatrix} \cos\varphi_1 \cos\varphi_2 & \sin\varphi_1 \cos\varphi_2 & \sin\varphi_2 \sin\phi \\ -\sin\varphi_1 \sin\varphi_2 \cos\phi & +\cos\varphi_1 \sin\varphi_2 \cos\phi & \\ -\cos\varphi_1 \sin\varphi_2 & -\sin\varphi_1 \sin\varphi_2 & \cos\varphi_2 \sin\phi \\ -\sin\varphi_1 \cos\varphi_2 \cos\phi & +\cos\varphi_1 \sin\varphi_2 \cos\phi & \\ \sin\varphi_1 \sin\phi & -\cos\varphi_1 \sin\phi & \cos\phi \end{bmatrix} \tag{5}$$

where the columns of a in equation (5) are given by the following expressions based on the miller indices of the desired orientation.

$$\hat{b} = \frac{(u,v,w)}{\sqrt{u^2+v^2+w^2}} \tag{6}$$

$$\hat{n} = \frac{(h,k,l)}{\sqrt{h^2+k^2+l^2}} \tag{7}$$

$$\hat{t} = \frac{\hat{n} \times \hat{b}}{\left|\hat{n} \times \hat{b}\right|} \tag{8}$$

We can set the vectors $\hat{b}$, $\hat{n}$, and $\hat{t}$ equal to the expression in eq. (5) to solve for φ_1, ϕ, and φ_2. Hence, for normal plane (hkl) and translating direction [uvw] the Euler angles are given by the following equations

$$\varphi_1 = \sin^{-1}\left(\frac{w}{\sqrt{u^2+v^2+w^2}} \frac{\sqrt{\left(h^2+k^2+l^2\right)}}{\sqrt{\left(h^2+k^2\right)}} \right) \tag{9}$$

$$\phi = \cos^{-1}\left(\frac{l}{\sqrt{h^2+k^2+l^2}} \right) \tag{10}$$

$$\varphi_2 = \cos^{-1}\left(\frac{k}{\sqrt{h^2+k^2}} \right) \tag{11}$$

These Euler angles are entered into ABAQUS [23] as material properties, and are read in by the UMAT code.

CHAPTER 3: FINITE ELEMENT MODEL

3.1 Geometry

The interfering asperities were modeled as cylinders, hence a 2D plane strain model was used. Even though this is not as realistic as spherical asperities, the characteristics of 2D simulations are comparable to 3D simulations [7] but with greatly reduced computational expense. Hence this initial study using continuum crystal plasticity considered the computationally less expensive 2D geometric approach, using the finite element (FE) method to solve for the response.

3.2 Boundary Conditions

Two general models were created for the studies conducted, one for the normal contact simulations and one for the sliding contact simulations. The models are based on the same geometry, meshing, and surface interactions, but the boundary conditions between the two are different.

The normal contact model was used for the mesh validation, and the normal contact elastic-plastic study. In this model the two cylinders were aligned about their vertical axes. The load is applied via displacement boundary conditions along the top surface of the upper cylinder, in 5 steps and then removed in 5 steps. The lower cylinder is held fixed by restraining the nodes along its bottom surface in the x and y directions and restraining the rotation in-plane. The base nodes of the upper cylinder are restrained in the x direction to stop relative tangential motion.

For the sliding contact study, interference is applied between the two cylinders with no contact. Then the upper cylinder is translated horizontally via displacement

boundary conditions as illustrated in Figure 12. Again the nodes along the bottom of the lower cylinder are completely restrained.

The interface at the surface was frictionless ($|\tau| = 0$), the upper cylinder's contact surface was defined as the master and the lower cylinder's contact surface was defined as the slave, with surface-to-surface enforcement specified at the interface. It should be noted that this surface-to-surface contact enforcement should be used rather than node-to-surface contact enforcement in order to avoid asymmetries between the upper and lower cylinders, even though it does cause an increase in computation time.

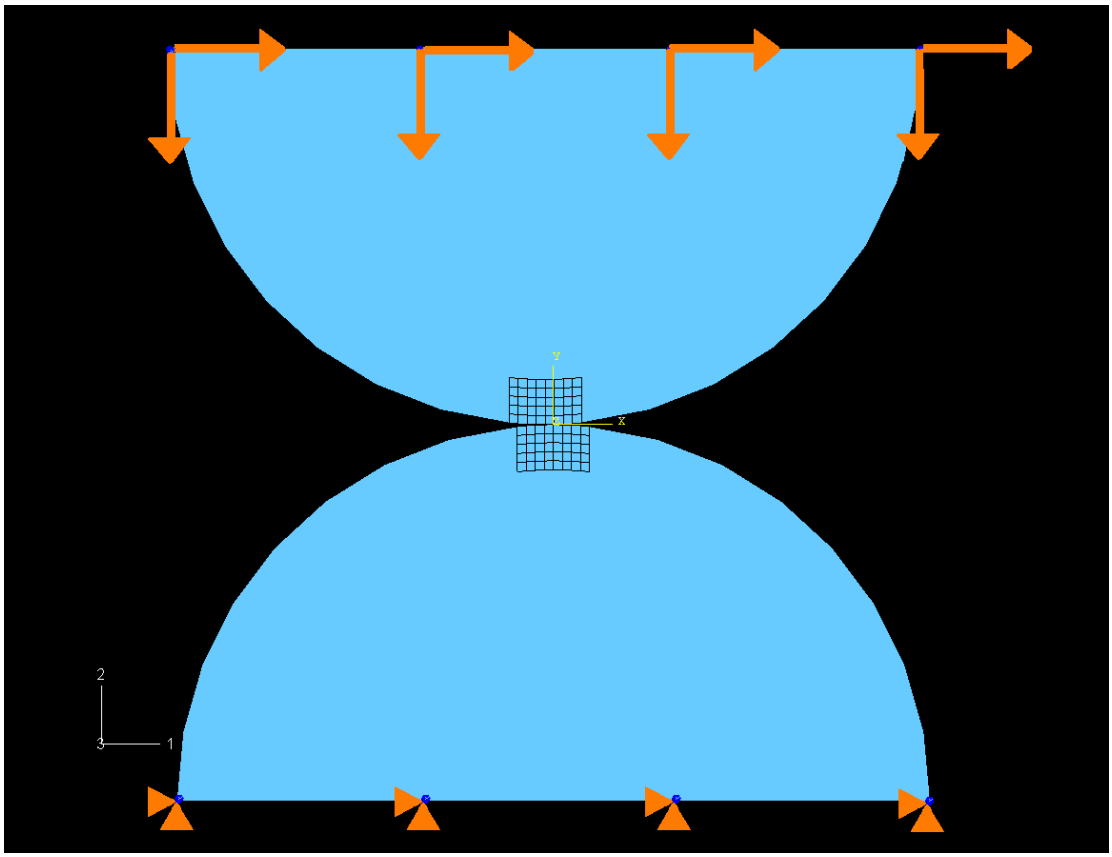

Figure 12: Boundary conditions for sliding contact simulation.

3.3 Loading

The interference ω is normalized to the minimum interference ω_c that will result in any plastic deformation according to the von Mises yield criterion assuming isotropic behavior (i.e., macroscopic polycrystalline response) [28]. This normalized interference is given the symbol ω*. All of the simulations conducted in this study were performed at ω*=20. This value was selected because it provided enough interference to allow the trends to be seen clearly yet it was low enough that the stress fields would not extend too deeply into the body requiring a larger densely-meshed region. It has been shown in previous works [7, 8] that at any ω*>1, the trends captured are the same but scale as a function of interference.

In the normal simulation the two cylinders have their longitudinal axes aligned. A displacement controlled load is applied in 5 steps and then removed in 5 steps. The load was ramped up to the maximum interference (ω*=20) and removed in even increments for these steps. This loading methodology was used for the mesh validation study, and also for the normal contact elastic-plastic simulations presented in Chapter 4.

In the sliding simulation the two cylinders are initially offset horizontally. Then the upper cylinder is translated horizontally via displacement boundary conditions. The translation of the top asperity was divided into 50 loading steps in ABAQUS, 25 load steps were used to bring the bodies into contact applying the load, and 25 load steps were used to bring the bodies back out of contact. The relative sliding position was normalized by the radius of the cylinder therefore when the cylinders are coming into contact $(x / R < 0)$, when the cylinders are aligned $(x / R = 0)$, and when the cylinders are

coming out of contact $(x/R > 0)$. The sliding simulations typically took approximately 48 hours on a PC with a single Intel Pentium 4 3.19 GHz processor and 2 GB of RAM.

3.4 Mesh and Validation

The elements used were four node linear rectangular plane strain elements (CPE4)[23]. The mesh convergence was evaluated by comparing the FE response using an elastic isotropic model with Hertz elastic pressure distribution and stress field. It is assumed that if the mesh is dense enough to accurately capture the elastic response it is sufficiently dense to capture the elastic-plastic response. The elements along the interface and in the crystal plasticity region are 5 μm square. The radius of the cylinders is 5mm. Thus the ratio of element size to radius is 1:1000. The optimized model has approximately 26000 elements. Outside of the region of interest quad-dominated elements, which are a combination of linear rectangular and linear tetrahedral elements, were used to smooth the mesh transition from dense to coarse as illustrated in Figure 13. Even though the mesh is not on a whole symmetric, it is symmetric in the region of interest and does not cause any asymmetries in the response.

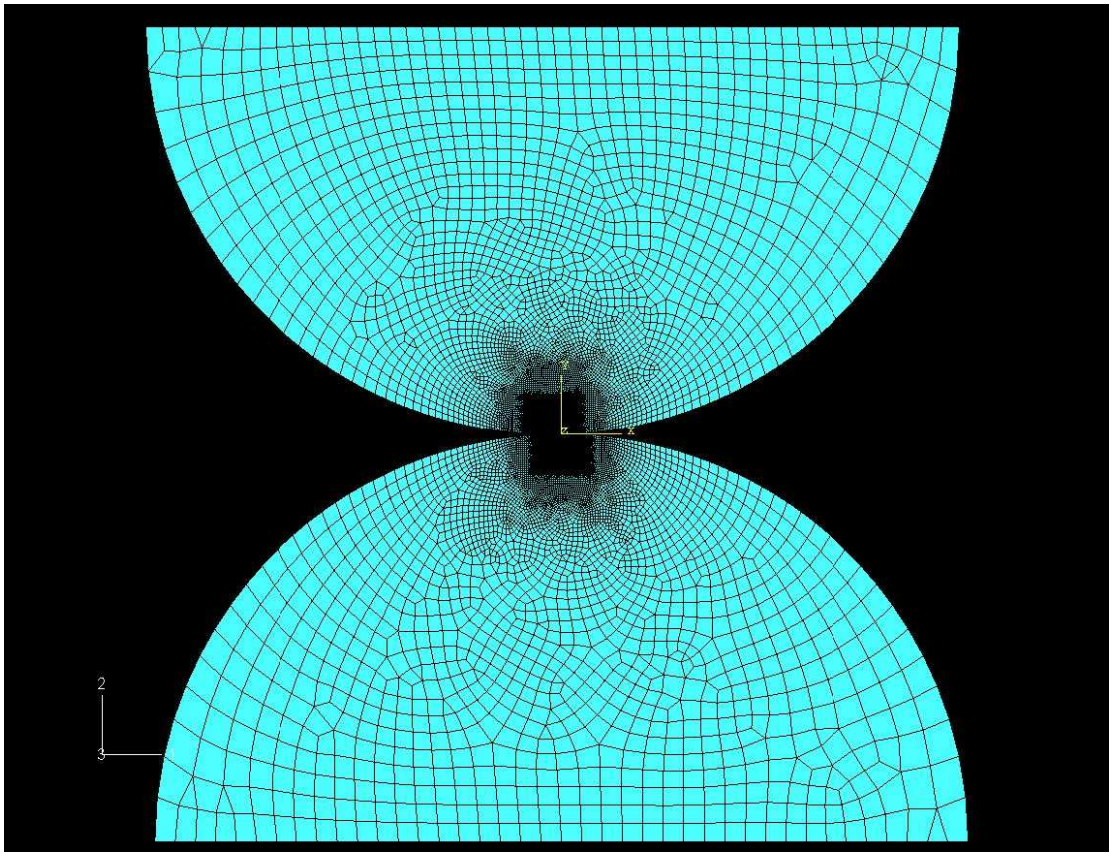

Figure 13: FE mesh of cylinders showing position when they first come into contact.

It should be noted that at the interference for which all the simulations are run, the plastic deformation is occurring in a small region relative to the size of the radius of the cylinder. Since the UMAT crystal plasticity code is computationally expensive, only the elements in the region where plastic deformation was expected were modeled using crystal plasticity. The crystal plasticity simulations typically ran for five times as long as the J_2 simulations. The size of the plasticity region, shown in Figure 14, was made large enough so there would be no effect of the boundary on the response. The remainder of the body was elastic. In all simulations shown, the stress levels at the boundary of the plastic region are below the initial yield of the crystal plasticity model, indicating completely elastic behavior.

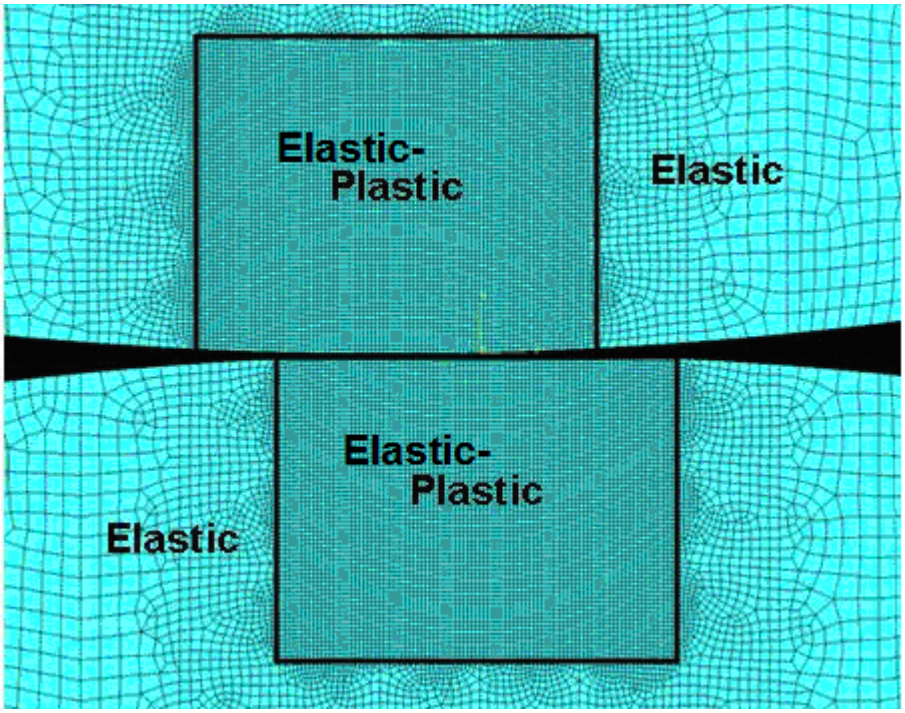

Figure 14: Zoomed in view of mesh.

The validation simulations shown were run for a normal contact load at a normalized interference $\omega^*=20$. There is a critical load P_c, defined in Section 4.5, which represents the normal load at which initial yield will occur under isotropic conditions. It should be noted that the relationship between critical interference (ω_c), and critical load is not exactly linear, $20\omega_c$ is equivalent to roughly $23.5P_c$. The material properties used for the validation were isotropic elastic properties of copper E=140GPa and ν=0.33. The simulations were run at smaller values of ω^* to ensure that the results are consistent at lower interferences. At lower interferences the mesh is not dense enough to accurately capture the response. Alternatively, the size of the elastic-plastic region would not be large enough to avoid boundary effects at higher interferences. In this sense the model is optimized for $\omega^*=20$.

Figure 15 shows the contact pressures obtained when running an entirely elastic simulation. Since at $\omega^*=20$ the response would normally be elastic-plastic, this is a

pseudo elastic response for validation purposes. The analytical values were calculated using P=10.763N/mm. It can be seen that the agreement of the contact pressure with the hertz analytical values is good. The calculated contact half-width a=0.021mm. There are 10 elements in the area of contact. The FE contact half width is a=0.025mm, yielding an error of roughly 19%. The difference between the FE contact width and the analytical contact width is caused by the spacing of the mesh. Ideally, the mesh needs to be denser in order to capture the edge of contact behavior. A mesh any denser would make the sliding contact simulations too computationally expensive. The resulting von Mises stress plot is shown in Figure 16. This is the response expected for an elastic contact between two cylindrical values as given by Hertz contact theory [29]. Based on the size of the elements, the maximum shear stress occurs at approximately 0.017mm below the surface. Based on the analytical values the maximum shear stress should occur at 0.016mm. The mesh generated is sufficiently dense to capture the stress and strain fields, which is one of the primary focuses of this study.

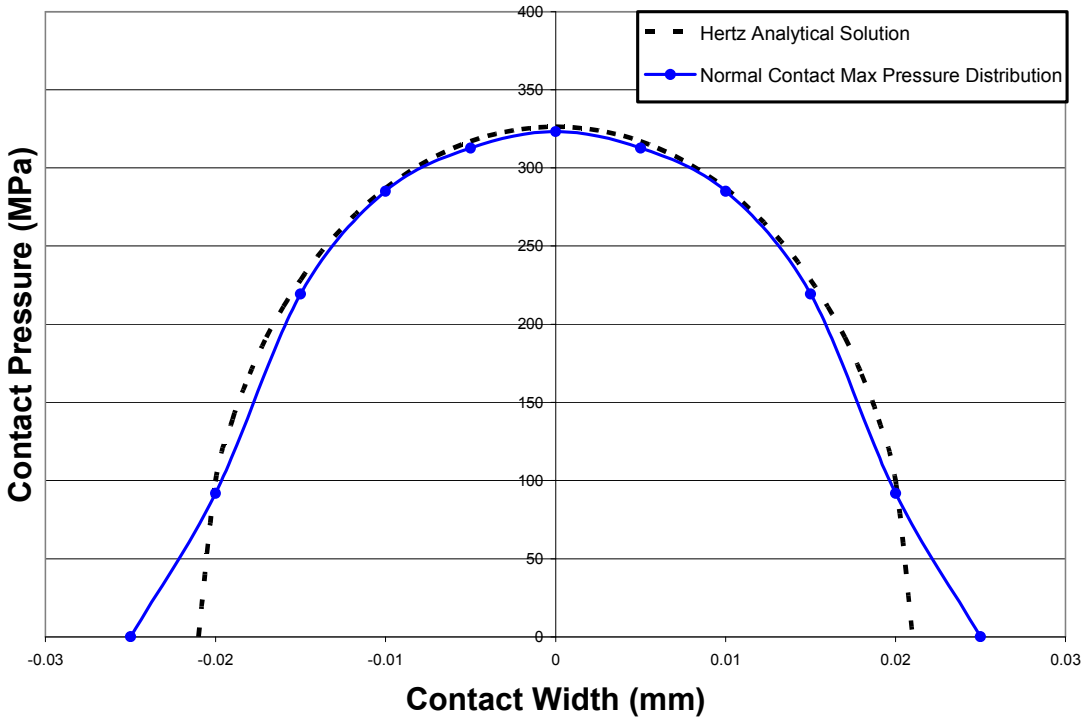

Figure 15: Elastic contact pressure validation at ω*=20.

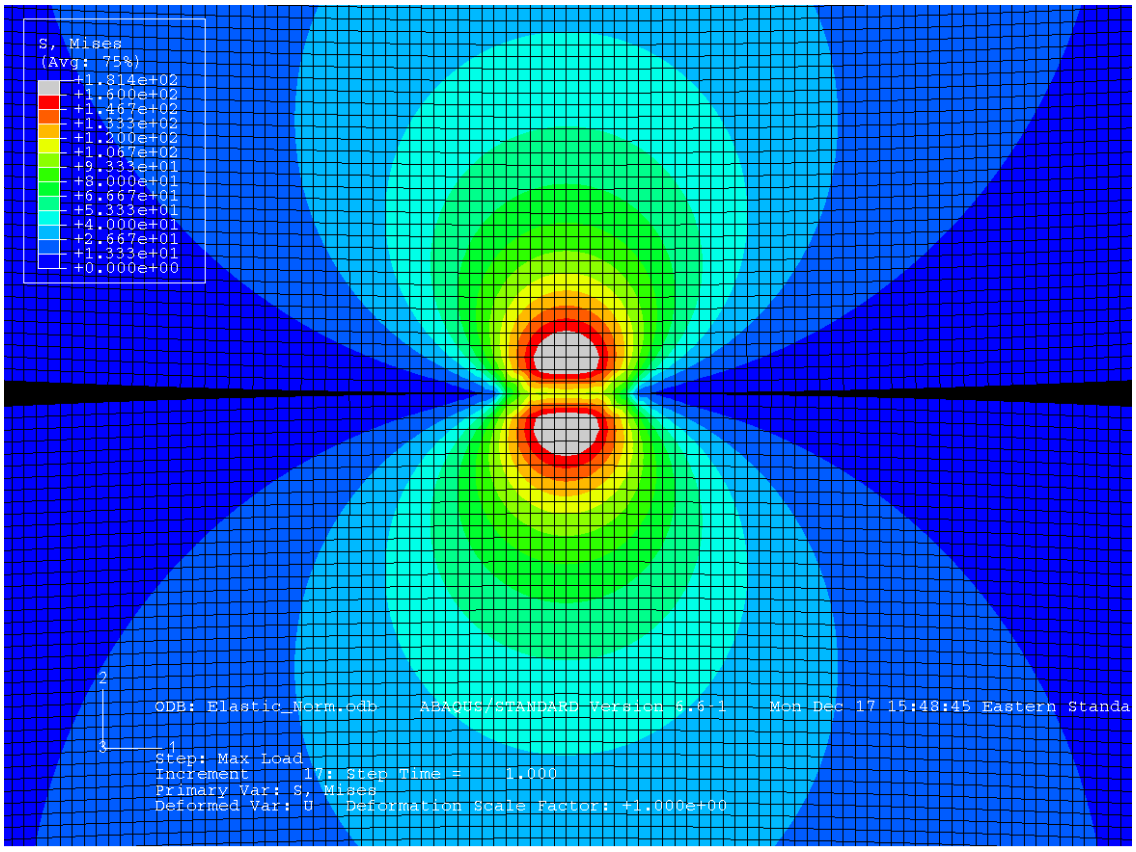

Figure 16: von Mises stress under normal contact at ω*=20.

CHAPTER 4: NORMAL CONTACT RESULTS & DISCUSSION

4.1 von Mises Stress: Max Load

The von Mises stress response for the isotropic on isotropic normal contact simulation is shown in Figure 17. The stress fields in the upper and lower bodies are symmetrical about both the vertical and horizontal axes. The shape of the stress fields is typical of a contact that uses an isotropic J_2 plasticity model, away from the contact interface the stress fields resemble that of the Hertz elastic response. However the stresses are more distributed since plasticity is taken into account. Figure 18 shows the von Mises stress response when loading on the (001) cube face oriented in two different orientations. The directions are perpendicular to the line of contact on the interface plane. In these simulations, both bodies are prescribed with the same orientations. The responses of these crystal plasticity simulations show clear differences from the simulation using the J_2 plasticity model, due in part to the anisotropic elastic constants. The normal loading on this plane results in well defined directions in which the stress is intensified. The $(001)[100]$ simulation shown in Figure 18(a) indicates that the stresses are highly concentrated and are not along the center axis of the contact, but to either side of the central axis. A pocket of lower stress is observed along the center axis of contact. When loaded in the $(001)[110]$ orientation, the stresses do not have the same magnitude as the $(001)[100]$ case, but they are more distributed throughout the body. The pocket of lower stress along the center axis is no longer observed and the response is more homogenous, though still considerable different than the isotropic J_2 plasticity case. Both of these cases are symmetric about both the vertical and horizontal axes.

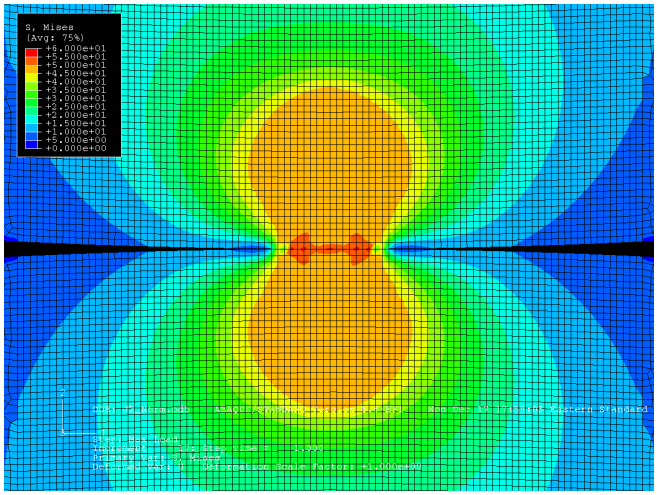

Figure 17: von Mises stress at maximum load for J_2 on J_2.

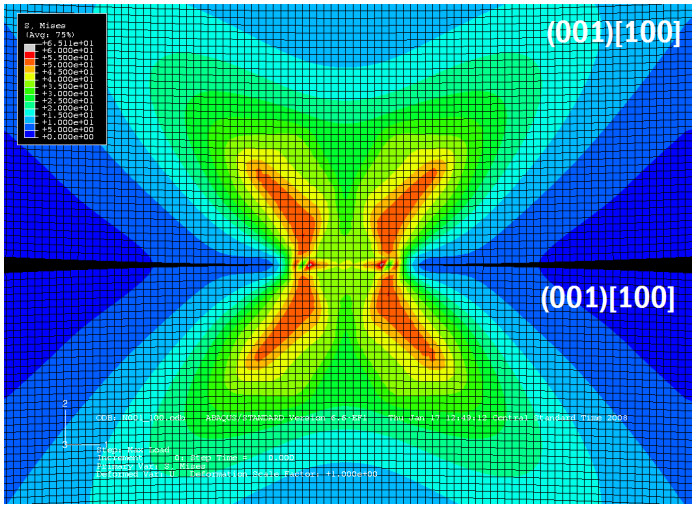

(a)

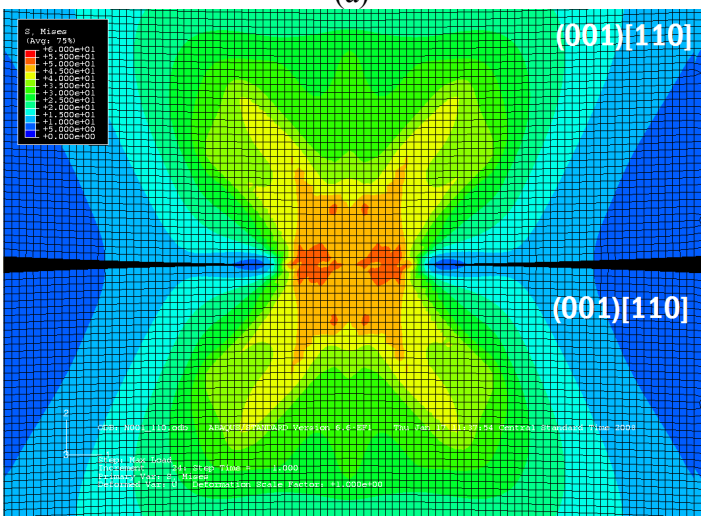

(b)

Figure 18: von Mises stress at maximum load for (a) (001)[100] on (001)[100] and (b) (001)[110] on (001)[110].

Normal loadings on the (110) plane are shown in Figure 19. The overall responses of these loading cases are symmetric as with the previous cases, as would be expected due to the symmetry of the crystals in contact. When loading in the $(110)[001]$ orientation, the magnitude of the stresses is lower. In Figure 19(a), again there is a pocket of low strain along the center axis of the contact near the surface, but near the edge of the contact there are areas of intensified stress. When studying the response of the $(110)[\bar{1}10]$, shown in Figure 19(c), it is observed that the stress response is identical to the case of loading on the $(001)[110]$ orientation. This leads one to believe that the slip systems are being activated in a similar manner causing a similar response. However, the $(110)[\bar{1}11]$ case shown in Figure 19(b), gives an interesting result, despite the symmetry in the problem and the simple normal loading, the stress fields are anti-symmetric, and no longer symmetric about the vertical or horizontal axis.

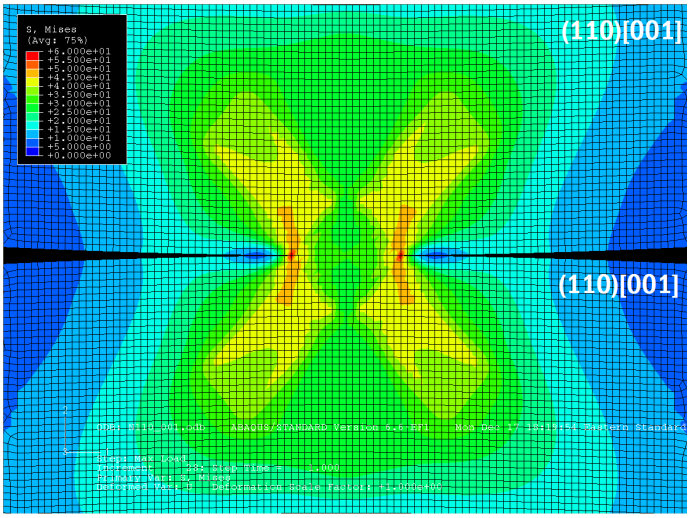

(a)

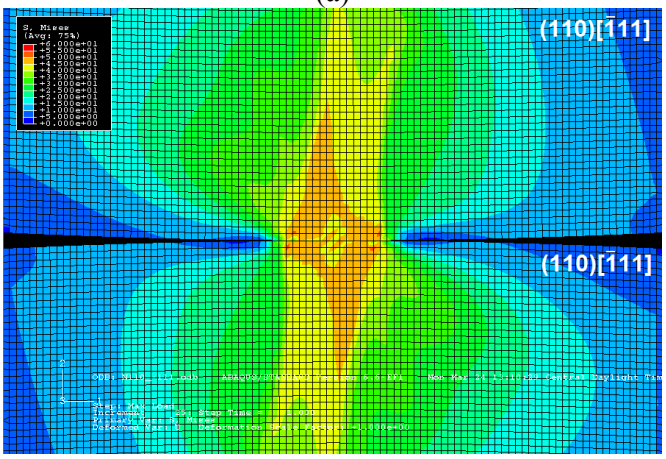

(b)

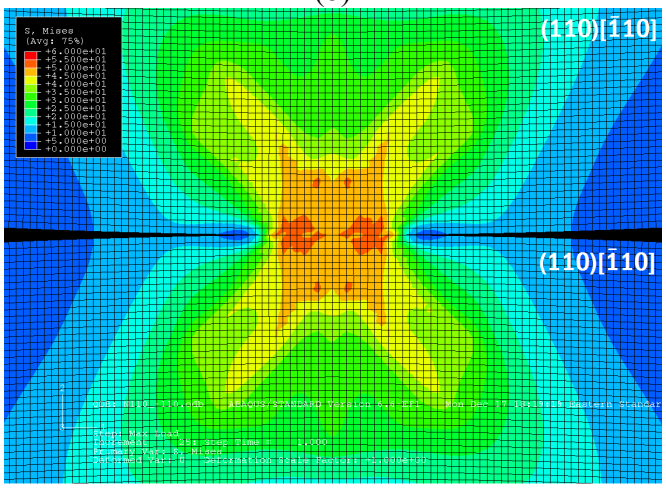

(c)

Figure 19: von Mises stress at maximum load for (a) $(110)[001]$ on $(110)[001]$ (b) $(110)[\bar{1}11]$ on $(110)[\bar{1}11]$ (c) $(110)[\bar{1}10]$ on $(110)[\bar{1}10]$.

The von Mises stresses for loading on the (111) plane are shown in Figure 20. When loading on this plane there are preferred locations of elevated stress such as those seen when loading on the (001) or (110) planes, but there are many more and they are much less diffuse. These plots are all symmetric about both the horizontal and vertical axes. The responses in the $(111)[\bar{2}11]$ and the $(111)[\bar{1}\,\bar{1}2]$ orientations are identical. Both of these simulations have a narrow pocket of less stress along the axis of symmetry, with the higher stresses occurring closer to the edge of contact. The $(111)[\bar{1}01]$ orientation is different. The location of highest stress is along the axis of symmetry. Although there are subtle differences in shape, the peak magnitude of the stresses in all of these simulations is the same.

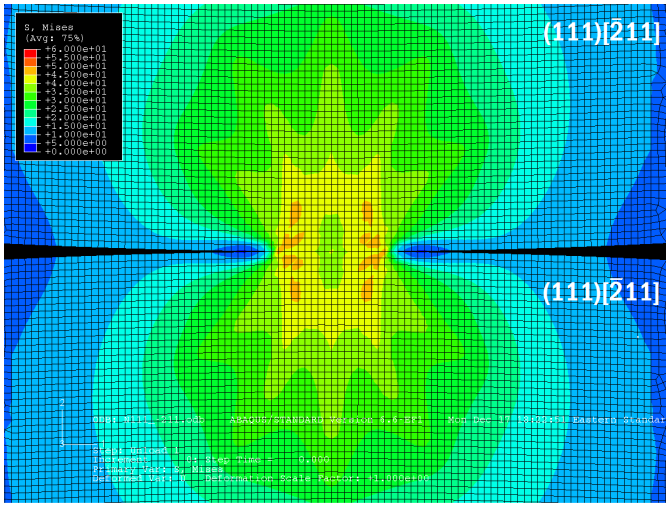

(a)

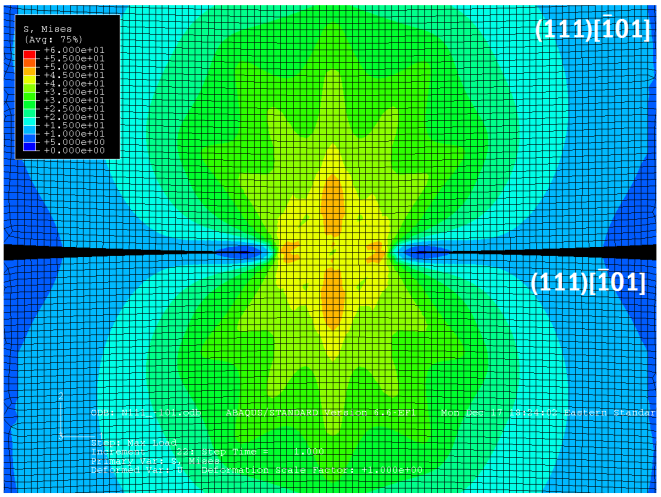

(b)

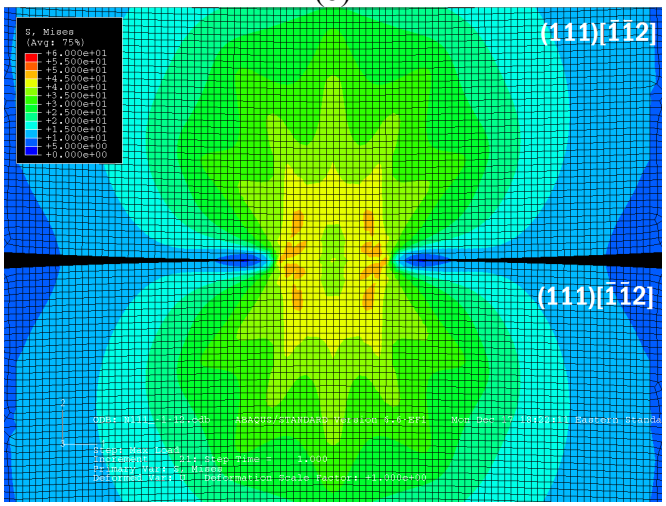

(c)

Figure 20: von Mises stress at maximum load for (a) $(111)[\bar{2}11]$ on $(111)[\bar{2}11]$ (b) $(111)[\bar{1}01]$ on $(111)[\bar{1}01]$ (c) $(111)[\bar{1}\,\bar{1}2]$ on $(111)[\bar{1}\,\bar{1}2]$.

It is important to note that the orientations selected for the majority of these simulations are extreme cases. In these orientations the lattice is often symmetric relative to the loading. The response of an orientation between one of these two extreme cases would be somewhere between. This is well demonstrated by the simulations loading on the (110) plane. The (110)[001] and $(110)[\bar{1}10]$ cases are perpendicular to each other. It has been shown that the response in these two perpendicular orientations are quite similar in terms of symmetry, but the $(110)[\bar{1}11]$ orientation which is at an angle between them is much different. We could expect this to be consistent with any other planes considered. In general, there are going to be two or more (based on the symmetries of the plane) extreme orientations with similar responses and the other orientations responses that fall somewhere in between. This is an example of one of the effects that can be captured using crystal plasticity models that cannot be captured using J_2 isotropic plasticity models.

4.2 Residual Stress

The residual stresses after the cylinders come out of contact for the J_2 simulations are shown in Figure 21, and for the crystal plasticity simulations in Figure 22-24. The plot is symmetric about the vertical and horizontal axes. Subsurface a pocket of low stress is formed, which was observed in all of the simulations. The highest stress areas are near the edge of the contact. The residual stresses for the simulations loading on the (001) plane are shown in Figure 22. The size of the residual stress fields is larger for the $(001)[110]$ orientation than when loading the $(001)[100]$ orientation. Also in Figure 22 one can see the evidence of the preferred directions on which the stress is higher,

mentioned in the previous section. However, since the elastic recovery has taken place, the magnitude of the stresses has fallen to a much lower level. The simulations on the (110) and (111) planes, shown in Figure 23 and 24, demonstrate similar features that were seen in the other cases. All of the simulations on these planes show a shape that is symmetric about both axes. The pocket of low stress takes on a heart shape, and for any given simulation one will notice small areas of higher residual stress. In general the plots with more residual stress have undergone more plastic deformation. The effects of these residual stress plots would become more interesting when looking at repeated loadings.

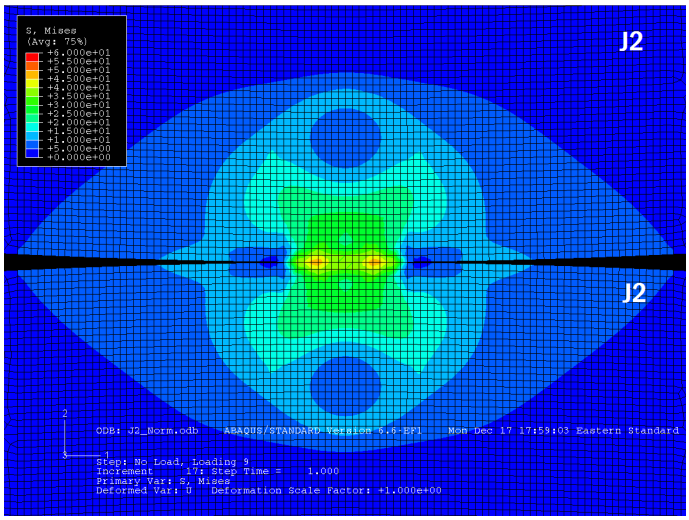

Figure 21: von Mises stress after loading isotropic on isotropic

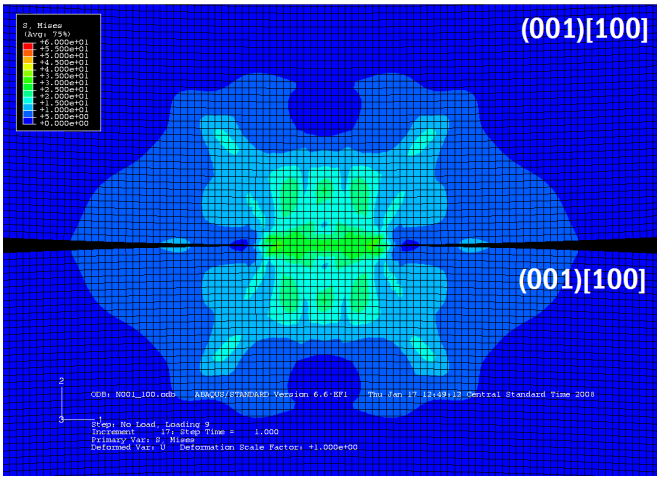

(a)

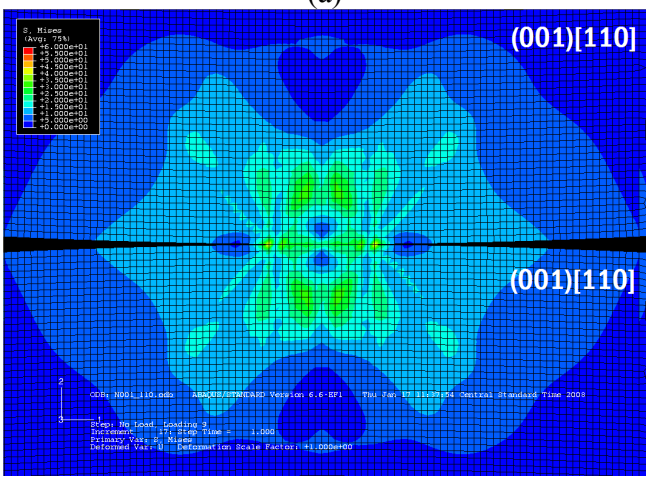

(b)

Figure 22: von Mises stress after loading (a) (001)[100] on (001)[100] and (b) (001)[110] on (001)[110].

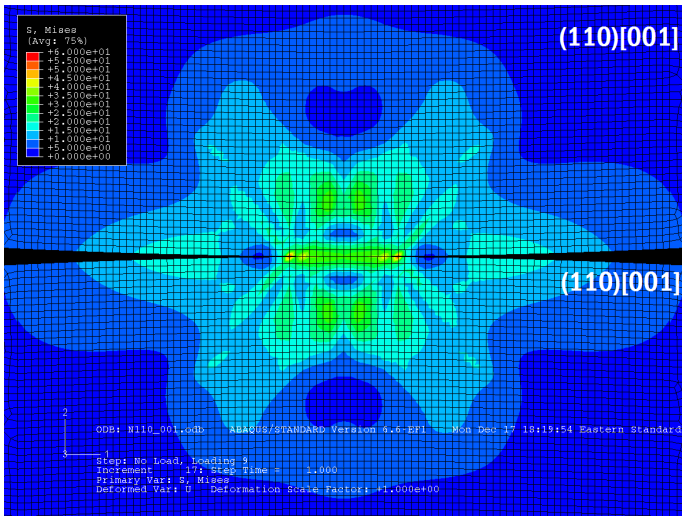

(a)

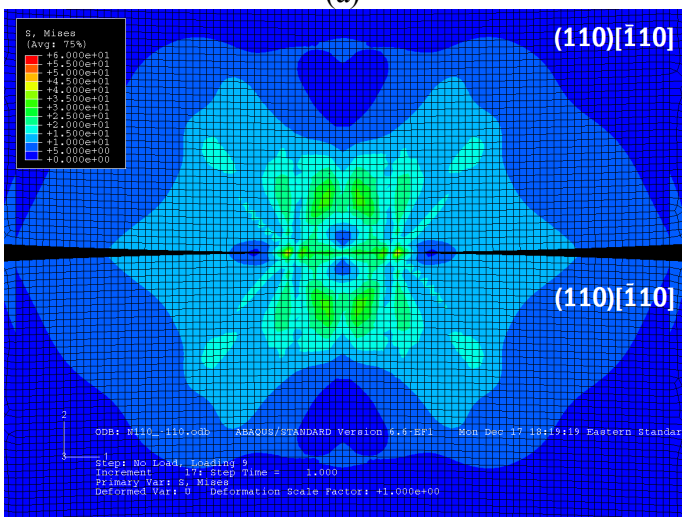

(b)

Figure 23: von Mises stress after loading (a) $(110)[001]$ on $(110)[001]$ (b) $(110)[\bar{1}10]$ on $(110)[\bar{1}10]$.

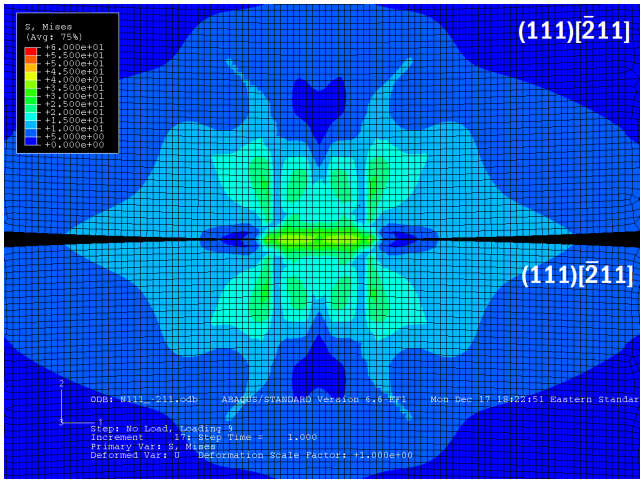

(a)

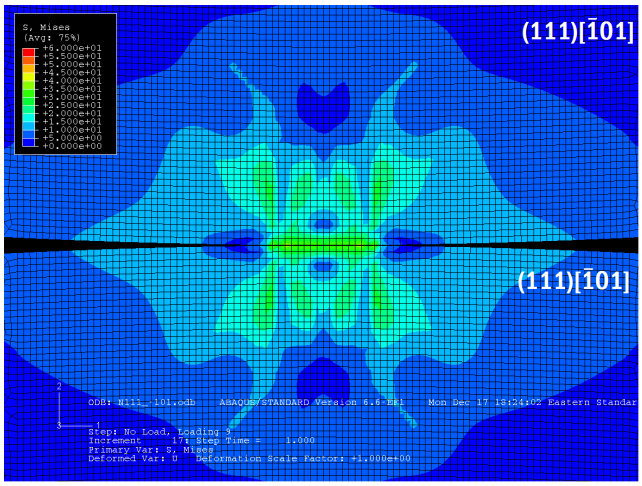

(b)

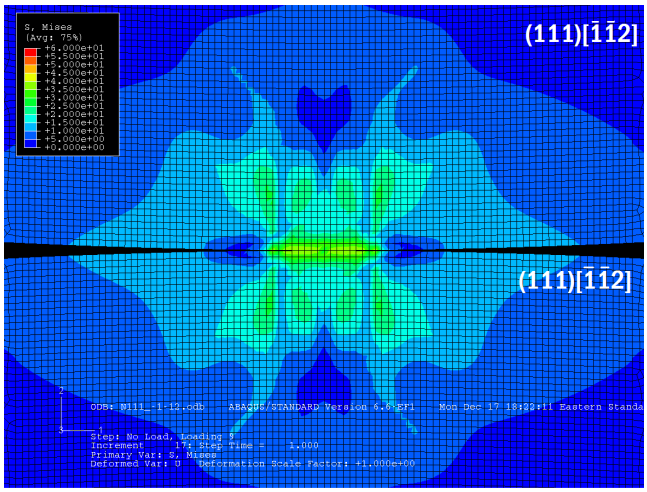

(c)

Figure 24: von Mises stress after loading (a) (111)[$\bar{2}$11] on (111)[$\bar{2}$11] (b) (111)[$\bar{1}$01] on (111)[$\bar{1}$01] (c) (111)[$\bar{1}\,\bar{1}$2] on (111)[$\bar{1}\,\bar{1}$2].

4.3 Residual Plastic Strain

The effective plastic strain after deformation is now examined. It is defined

$$\bar{\varepsilon}^{p} = \sqrt{\frac{2}{3}\varepsilon_{ij}^{p}\varepsilon_{ij}^{p}}\,, \tag{12}$$

Figure 25 shows the residual effective plastic strain under normal loading for the J_2 simulation. The majority of the plastic strain accumulates near the edge of contact where the stresses are the highest, with a band of intensified strain that occurs at a 45 degree angle from the center subsurface to the edge of the contact on the surface. There is however no strain at the surface in the center of the contact, where the hydrostatic stress is high. The plastic strain plots using crystal plasticity show a much different trend than when using the J_2 model. The simulations on the (001) plane, shown in Figure 26, show that the majority of plastic strain occurs subsurface, peaking along the line of symmetry. Much more plastic strain is observed in the $(001)[110]$ case than in the $(001)[100]$. The bands which were present in the J_2 simulations are also present in these simulations and they are very pronounced in the $(001)[110]$ case.

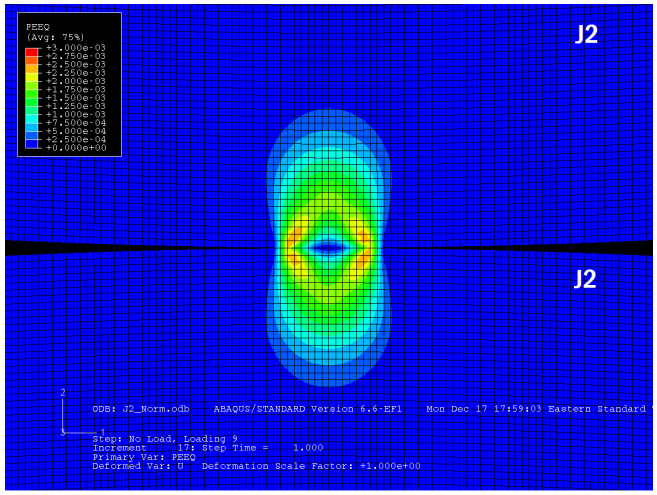

Figure 25: Residual effective plastic strain for J_2 on J_2.

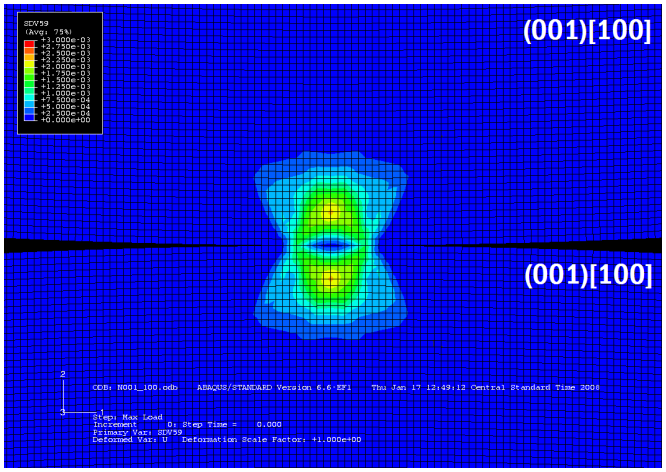

(a)

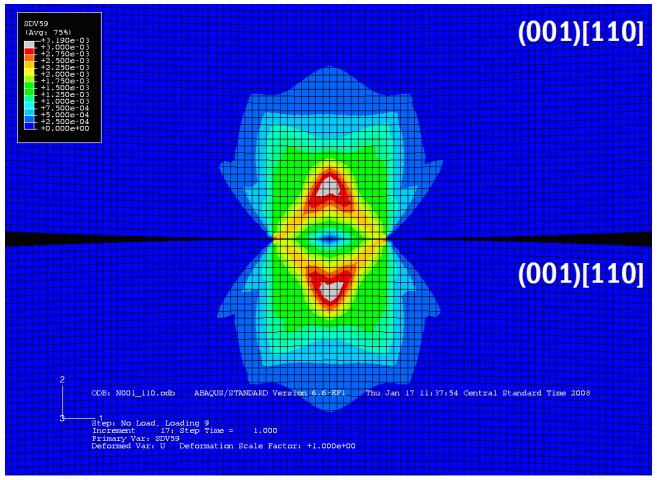

(b)

Figure 26: Residual effective plastic strain for (a) (001)[100] on (001)[100] and (b) (001)[110] on (001)[110].

Shown in Figure 27, when loading on the (110) plane the shapes are similar between loading the $(110)[001]$ orientation and the $(110)[\bar{1}10]$ orientation, but they do not differ nearly as much as when loading on the (001) plane. Though the magnitude is a little higher in the $(110)[\bar{1}10]$ case. However, the $(110)[\bar{1}11]$ orientation has a completely different shape from the other two cases, and it can be seen that the strain response is anti-symmetric just as the von Mises stress. When loading on the $(111)[\bar{2}11]$, $(111)[\bar{1}01]$, and $(111)[\bar{1}\,\bar{1}2]$ orientations, shown in Figure 28, the response of the effective plastic strain is nearly identical, even though there were subtle differences in the von Mises stress plots between the three different cases. Also in these plots the maximum does not occur subsurface along the line of symmetry but near the surface at the edge of contact.

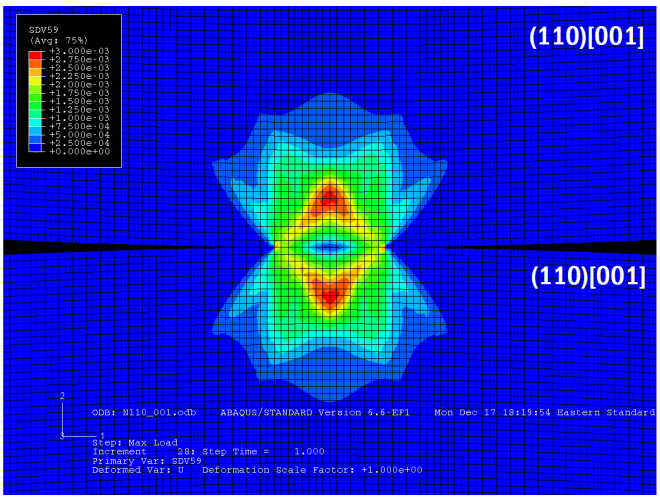

(a)

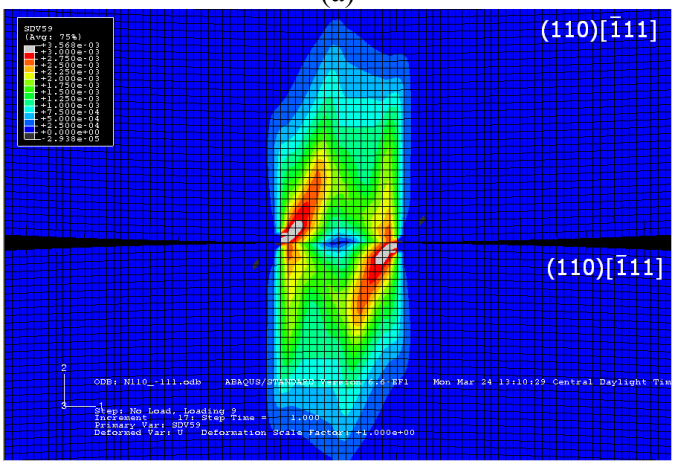

(b)

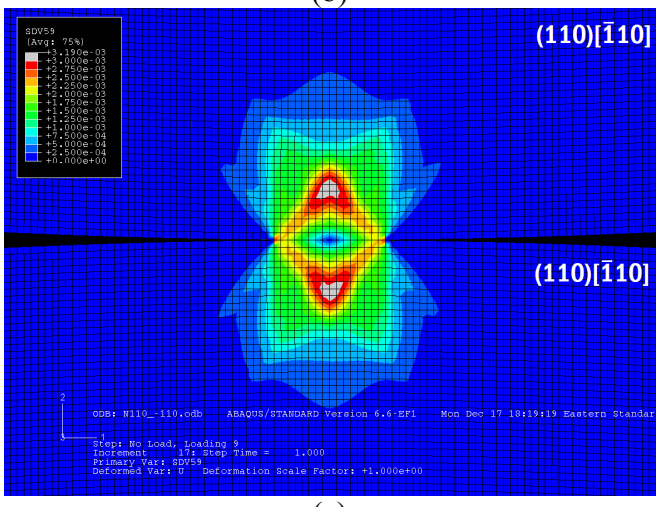

(c)

Figure 27: Residual effective plastic strain for (a) $(110)[001]$ on $(110)[001]$ (b) $(110)[\bar{1}11]$ on $(110)[\bar{1}11]$ (c) $(110)[\bar{1}10]$ on $(110)[\bar{1}10]$.

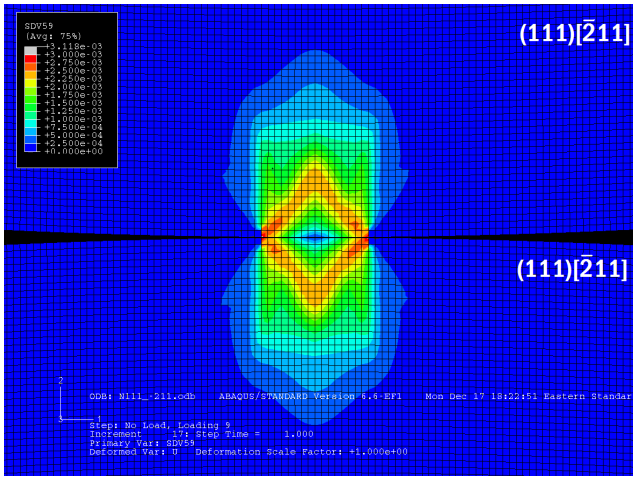

(a)

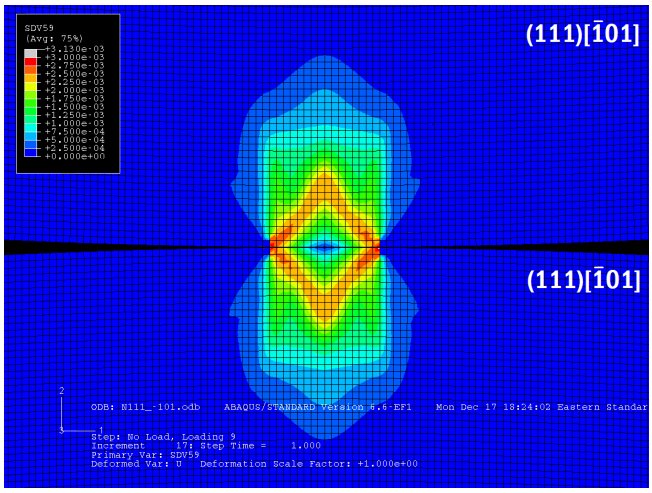

(b)

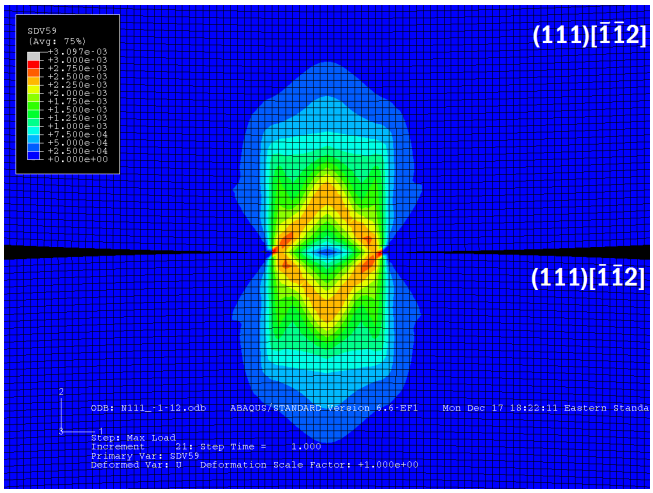

(c)

Figure 28: Residual effective plastic strain for (a) $(111)[\bar{2}11]$ on $(111)[\bar{2}11]$ (b) $(111)[\bar{1}01]$ on $(111)[\bar{1}01]$ (c) $(111)[\bar{1}\,\bar{1}2]$ on $(111)[\bar{1}\,\bar{1}2]$.

General trends have been observed for all of the orientations run, but several issues need to be discussed as it pertains to a real engineering problem. If we examine the $(110)[\bar{1}11]$ orientation we see that it has a higher magnitude of effective plastic strain, and the location of this maximum strain is at the surface rather than subsurface as in the other two (110) plane cases. Based on the rotation of the lattice to different orientations, the location of the maximum effective plastic strain may change quite significantly. This is important as it pertains to a distribution of asperities, one cannot assume that the maximum plastic strain will occur in the same location for all asperities. The magnitude and location of maximum plastic strain will change based on the orientation of each asperity. This has implications in mechanisms which are based on magnitude and location of plastic strain, such as crack formation.

4.4 Active Slip Systems

To better understand the behavior of the asperities under normal loading for different orientations it is helpful to output which slip systems are active for each orientation, shown in Table 1. The values in this table were obtained by summing the strain increment on each slip system from the start of the simulation to the maximum interference, including all of the sub-increments run in the UMAT. The maximum magnitude values from the nodes in the elastic-plastic region were taken from the last loading step of the simulation. The numerical values do not have a physical meaning but this method does allow us to clearly distinguish between the active and inactive slip systems. For the purposes of discussion the highly active slip systems are defined as those whose magnitude is greater than or equal to 0.4, and inactive slip systems (i.e. less

active) are those whose magnitude is less than 0.4. To make the table easier to interpret the active slip systems are highlighted in green.

For loading in the (001)[100] orientation the majority of the slip systems are active, yet the plastic deformation that occurs in this case is significantly less than when loading the (001)[110] orientation, which has far fewer active slip systems. However, the magnitude of accumulated plastic strain on a given active slip system in the (001)[110] orientation is much higher. Hence, the extent and magnitude of plastic deformation is more dependent on the magnitude of accumulated plastic strain than the number of slip systems being activated. Interestingly, the slip systems in the $(111)[\bar{2}11]$ and $(111)[\bar{1}\bar{1}2]$ orientations are different as one might expect, yet the overall response of these two cases is identical.

Table 1: Aggregate accumulated plastic strain metric on each slip system.

		Simulation							
		(001)[100]	(001)[110]	(110)[001]	(110)[-111]	(110)[-110]	(111)[-211]	(111)[-101]	(111)[-1-12]
Slip System	(111)[-110]	0.465	0.847	-0.042	0.000	-0.003	0.016	0.097	0.006
	(111)[0-11]	-0.323	-0.847	-0.830	-0.481	1.022	0.237	-1.987	2.594
	(111)[10-1]	-0.451	0.000	0.830	-0.481	-1.022	-0.009	0.000	-0.142
	(-111)[-1-10]	-0.465	0.004	0.154	1.497	-0.156	0.479	0.552	-0.684
	(-111)[101]	0.493	-0.141	-0.008	-0.042	-0.005	-0.469	0.075	0.118
	(-111)[01-1]	0.296	-0.005	0.009	0.000	0.004	0.079	-0.569	0.692
	(-1-11)[1-10]	0.465	-0.005	-0.010	0.000	-0.025	-0.004	-0.027	-0.012
	(-1-11)[011]	-0.323	0.004	-0.695	1.200	0.892	0.116	0.027	0.020
	(-1-11)[-10-1]	-0.451	-0.141	0.695	-1.200	-0.892	-2.014	-0.262	0.353
	(1-11)[110]	-0.465	-0.959	-0.154	-1.497	0.156	-1.802	-2.197	2.913
	(1-11)[-101]	0.493	0.001	-0.009	0.000	0.007	-0.004	0.000	-0.162
	(1-11)[0-1-1]	0.647	2.470	0.022	0.071	0.016	0.296	0.191	0.011

4.5 Normal Force

Since the loading is displacement controlled, the normal force will vary depending on the deformation behavior. The normal force plotted as a function of interference during the simulations is shown in Figure 29. The normal reaction force, F_y

is normalized by the critical load P_c. The critical load P_c is the normal force at the onset of yielding if the two cylinders are brought into contact without any tangential load. It is determined from an elastic contact analysis using the von Mises yield criterion as described in Green [28], and given by the following,

$$\frac{P_c}{L} = \frac{\pi R\left(CS_y\right)^2}{E'} \tag{13}$$

where R is the effective radius for two cylinders of radii R_1 and R_2 given by

$$R = \left(\frac{1}{R_1} + \frac{1}{R_2}\right)^{-1}, \tag{14}$$

E' is the effective elastic modulus given by,

$$E' = \left(\frac{1-\nu_1^2}{E_1} + \frac{1-\nu_2^2}{E_2}\right)^{-1} \tag{15}$$

where E_1 & E_2 are the elastic modulii and ν_1 & ν_2 are the Poisson's ratios of cylinders 1 and 2 respectively. In Eq. 13, S_y is the yield strength of the material assuming isotropic behavior, here S_y=37MPa. C is a constant that depends on Poisson's ratio, if $\nu \geq 0.1938$, C is calculated by the following expression;

$$C = 1.164 + 2.975\nu + 2.906\nu^2 \tag{16}$$

here, C = 1.83. Since this is a plane-strain study, the critical load P_c is defined per length L.

As previously mentioned load steps 1 to 5 increase the interference to a maximum of ω*=20, and then load steps 6 to 10 remove the interference. The elastic response is a perfect linear increase and decrease and follows the same path upon unloading as during loading. The plastic simulations do not reach the same normal force as the elastic

simulation since plastic deformation is occurring. In the plastic simulations a hysteresis is observed, upon unloading the normal force decreases at a higher rate than it increased during loading. The J_2 plasticity case reached a higher normal force than the crystal plasticity cases. This may be attributed to the aggregate yield strength for an isotropic model taking into account intergranular constraints that determine the plastic properties for the isotropic model. Comparing the plots for the crystal plasticity simulations loading on the (001) plane, shown in Figure 29(a), the (001)[100] orientation reached a higher normal force than the (001)[110] orientation. This indicates more deformation in the latter case resulting in a lower peak normal reaction force and a steeper slope upon unloading. Figure 29(b) shows the normal reaction forces for the simulations on the (110) and (111) planes. It can be seen that there is very little variation in these cases. Even though the overall force responses are similar between many of the orientations, locally there can be large variations in the stress and strain responses.

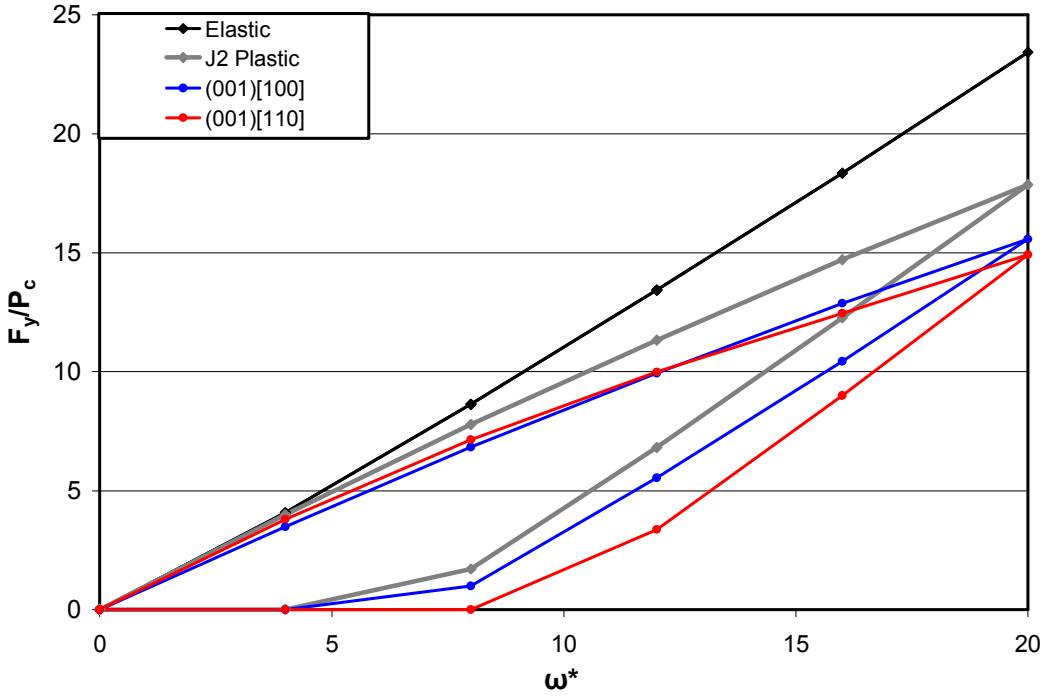

(a)

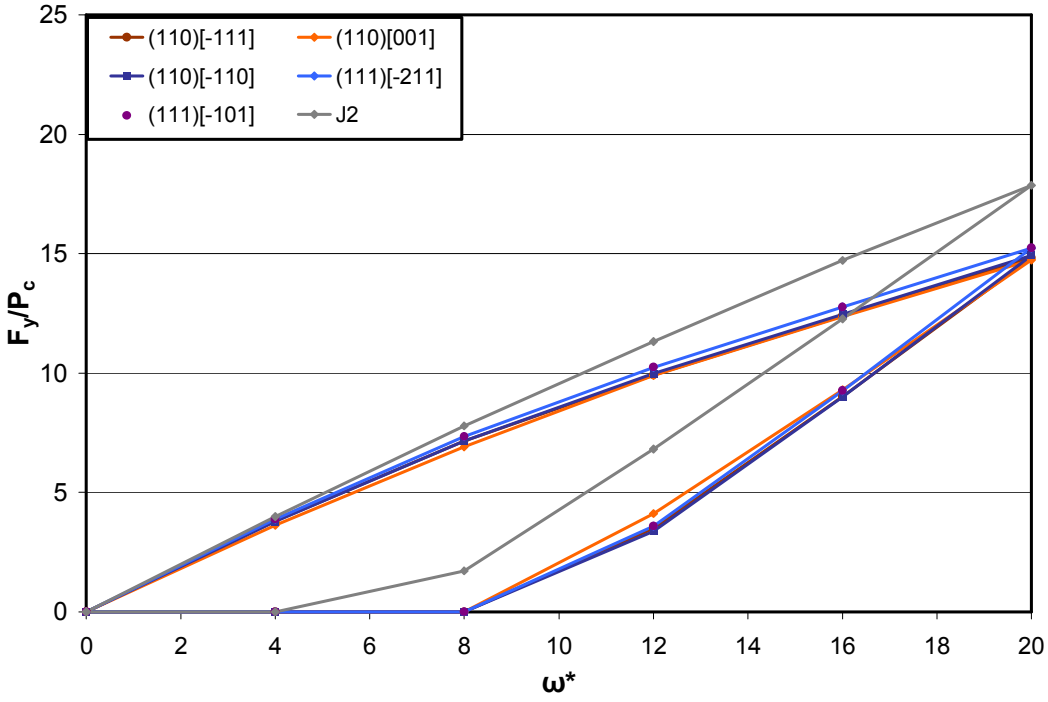

(b)

Figure 29: Normal reaction force during load steps on the (a) (001) plane (b) (110) and (111) plane.

CHAPTER 5: SLIDING CONTACT RESULTS & DISCUSSION

5.1 Strains

The effective plastic strains as defined in eq. (12) after completely translating the cylinders horizontally for the interference $\omega^*=20$ for various material cases are shown in Figure 30-33. The isotropic J_2 plasticity is shown in Figure 30. For the crystal plasticity simulations, the cylinders are single crystals with the normal of the specified plane oriented in the vertical direction in Figure 4 and the orientation of the crystal in the specified translating direction. On the (001) cube face translating in the $\langle 100 \rangle$ and $\langle 110 \rangle$ directions are shown in Figure 31(a) and (b) respectively. The deformations in these cases are quite different. First, as expected, the effective plastic strains are anti-symmetric in all three cases since both cylinders in each case are the same material. The contours of the effective plastic strain field for the J_2 simulation are smoother than the crystal plasticity simulations. Additionally, the J_2 simulation predicts a higher magnitude of effective plastic strain than the crystal plasticity simulations. The initial yield strength on an individual slip system (13 MPa) in the crystal plasticity model is smaller than the yield strength in the J_2 plasticity model (37 MPa). Hence, plastic deformation can occur more easily in crystal plasticity if the slip system is favorably oriented. Again, it should be emphasized that the macroscopic polycrystalline response predicted by the J_2 plasticity and crystal plasticity models is the same (Figure 7). Crystal plasticity provides a considerably more realistic representation of the local plastic strains. As one might expect, the orientation of the crystal with respect to the translating direction significantly

affects the deformation response. The maximum effective plastic strain is 21.5% greater when translating in the ⟨110⟩ direction compared to the ⟨100⟩ direction.

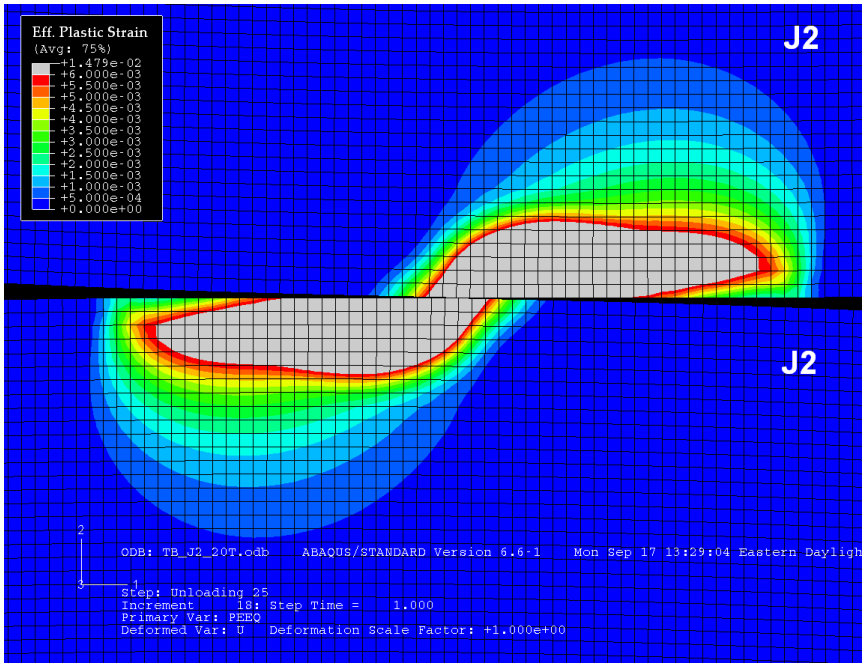

Figure 30: Effective plastic strain after translating cylinders with $\omega^* = 20$ for isotropic over isotropic.

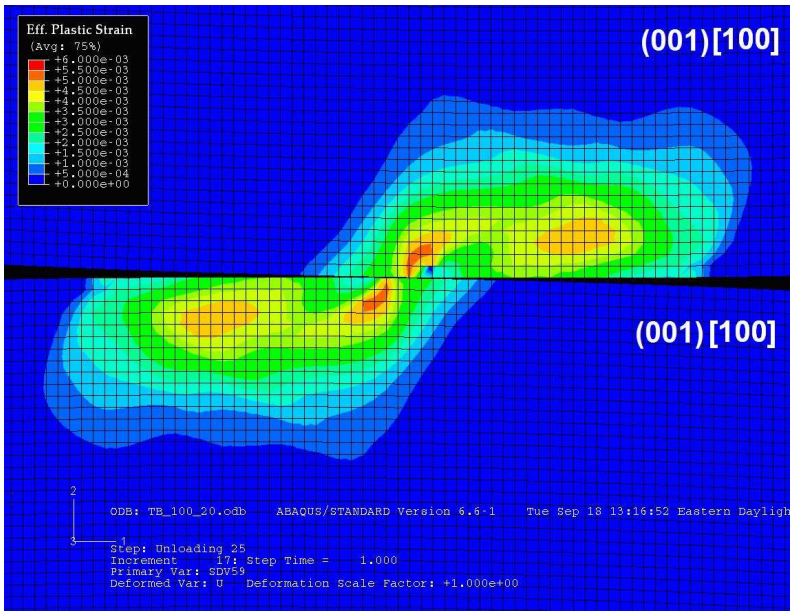

(a)

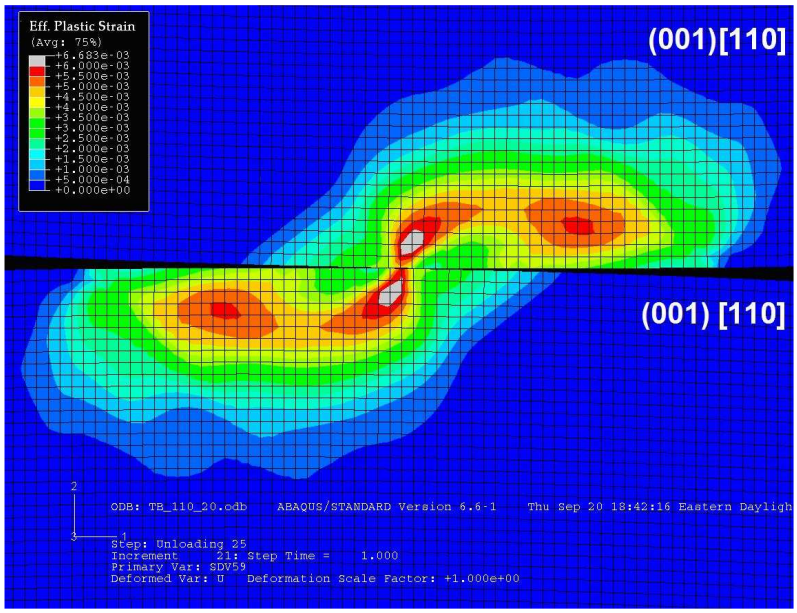

(b)

Figure 31: Effective plastic strain after translating cylinders with $\omega^* = 20$ for (a) (001)[100] over (001)[100] (b) (001)[110] over (001)[110].

The results of the simulations normal to the (110) plane translating in the [001], $[\bar{1}11]$, and $[\bar{1}10]$ directions are shown in Figure 32. The magnitude and shape of the effective plastic deformation is similar when translating in the [001] and translating in the $[\bar{1}10]$ simulations, the latter undergoing slightly more deformation. However, when translating in the $[\bar{1}11]$ there is much less magnitude of effective plastic strain occurring. Compare this to the normal contact simulation for this same orientation where the magnitude of effective plastic strain was higher in the $(110)[\bar{1}11]$ orientation than the other two orientations on the (110) plane. Sliding has the opposite effect on the (110) $[\bar{1}11]$ orientation, it decreases the maximum effective plastic strain relative to the (110)[001] and the (110) $[\bar{1}10]$ orientations. These are the types of effects that cannot be captured using isotropic plasticity models.

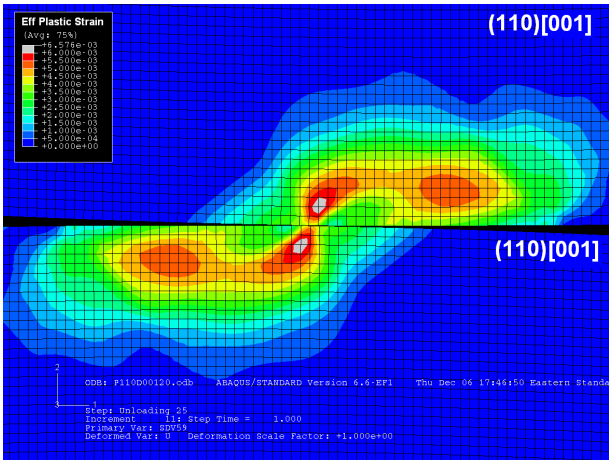

(a)

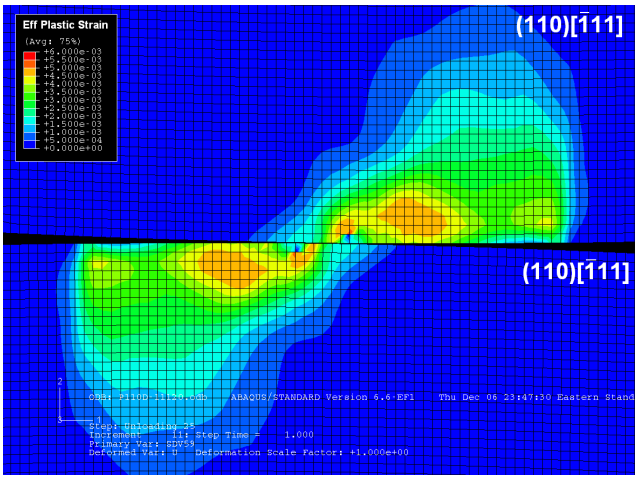

(b)

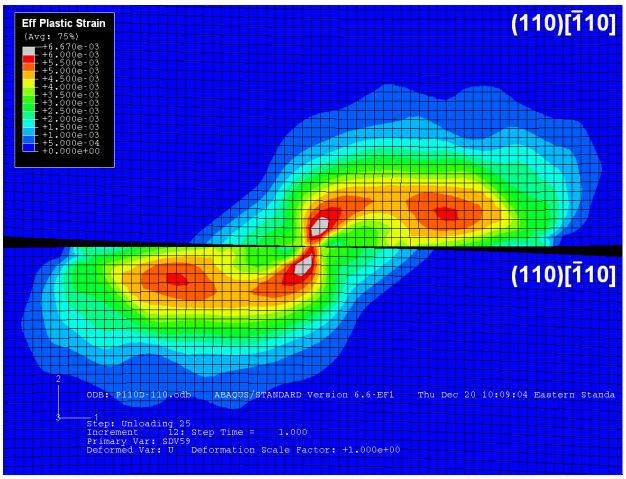

(c)

Figure 32: Effective plastic strain after translating cylinders with $\omega* = 20$ for (a) $(110)[001]$ over $(110)[001]$ (b) $(110)[\bar{1}11]$ over $(110)[\bar{1}11]$ (c) $(110)[\bar{1}10]$ over $(110)[\bar{1}10]$.

The effective plastic strains for the simulations normal to the (111) plane translating in the $[\bar{2}11]$, $[\bar{1}01]$, and $[\bar{1}\bar{1}2]$ directions are shown in Figure 33. It can be seen that the responses for the three different orientations are identical. Both the magnitudes and shapes of the fields are the same for all three cases. This does not agree with the expected response based on the experimental results [15]. Translating in the $[\bar{2}11]$ should have the minimum plastic deformation, translating in the $[\bar{1}\bar{1}2]$ should have the maximum plastic deformation, and translating in the $[\bar{1}01]$ should fall somewhere in between. It is hypothesized that in order to capture this effect latent hardening may need to be included in the crystal plasticity model.

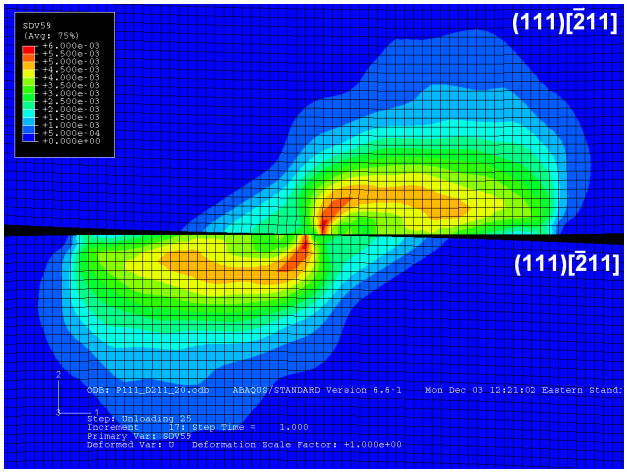

(a)

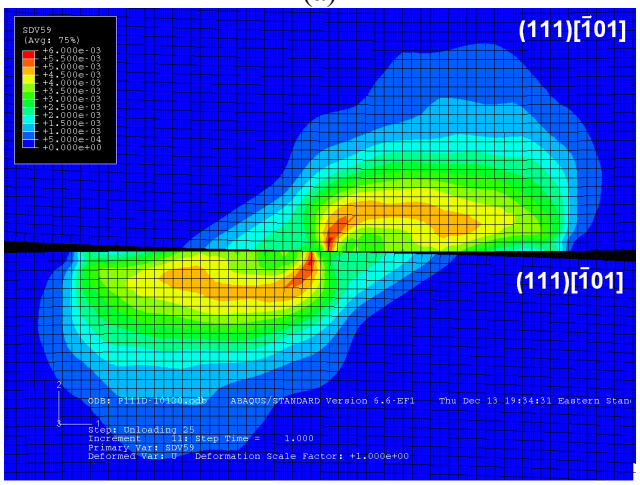

(b)

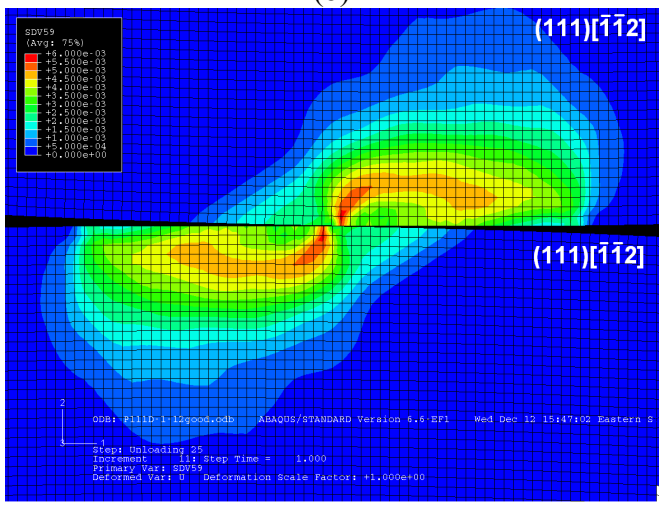

(c)

Figure 33: Effective plastic strain after translating cylinders with $\omega* = 20$ for (a) (111)[$\bar{2}$11] over (111)[$\bar{2}$11] (b) (111)[$\bar{1}$01] over (111)[$\bar{1}$01] (c) (111)[$\bar{1}\,\bar{1}$2] over (111)[$\bar{1}\,\bar{1}$2]

For the same vertical interference (ω) the magnitude of effective plastic strain is between two and three times greater depending on the orientation in sliding than under normal loading for the crystal plasticity simulations. For the isotropic J_2 model the magnitude difference is even greater, almost six times higher in the sliding case. The increase in plastic strain is caused by increased shearing forces during sliding. Since the isotropic model is based solely on the maximum shear stress, the effect of sliding on this case is very pronounced. However, in the crystal plasticity model, the amount of deformation that occurs on a slip system is dependent on resolved shear stress on that slip system. For a given orientation, the additional shearing force from sliding causes more strain to occur only on certain slip systems, it does not affect them all equally. Since the effective plastic strain is based on the strain of all of the slip systems, the crystal plasticity model is less sensitive to the added shear force from sliding than the isotropic J_2 model.

5.2 Stresses

5.2.1 Max Vertical Interference

There is also a considerable difference in the stress response for the previously mentioned cases as shown in Figure 34-36. Here, the von Mises stress when the two cylinders are vertically aligned (x/R = 0) is shown. The crystal plasticity models show that the stresses are localized in intense bands in the crystal and hence plastic strains are also localized during deformation. When normal to the (001) plane translating in the ⟨100⟩ direction, the peak stress is higher and the stresses are more intensified in bands than when translating in the ⟨110⟩ direction. More plastic deformation occurs in the latter case resulting in additional stress redistribution and hence a reduction in the elevation of

the local stress. These bands are more intense when there is less plastic deformation or in other words the crystal is in a "harder" orientation. Obviously, the isotropic J_2 simulations cannot capture any of these variations in the stress fields with orientation and in fact the stress field for that case looks completely different. It should be noted that the isotropic J_2 simulations compare favorably to those conducted by Vijaywargiya and Green (Figure 5) [8]. However, the results will not match exactly since our plasticity model is describing annealed Cu which has a considerably lower initial yield strength and much higher rate of hardening than the elastic-perfectly plastic model used by them.

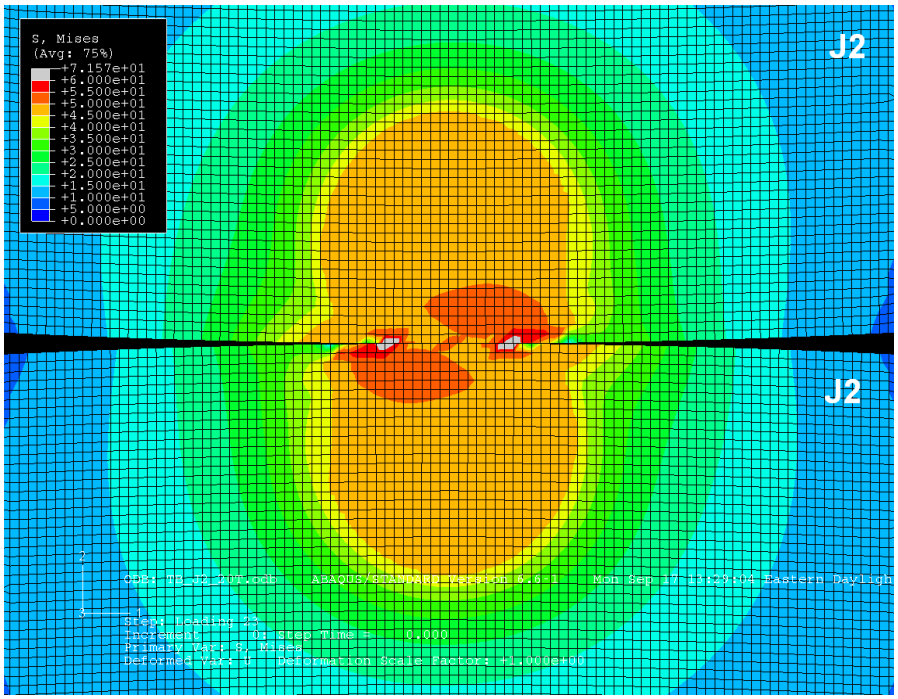

Figure 34: Von Mises stress at maximum vertical interference (x/R = 0) with ω* = 20 for isotropic over isotropic

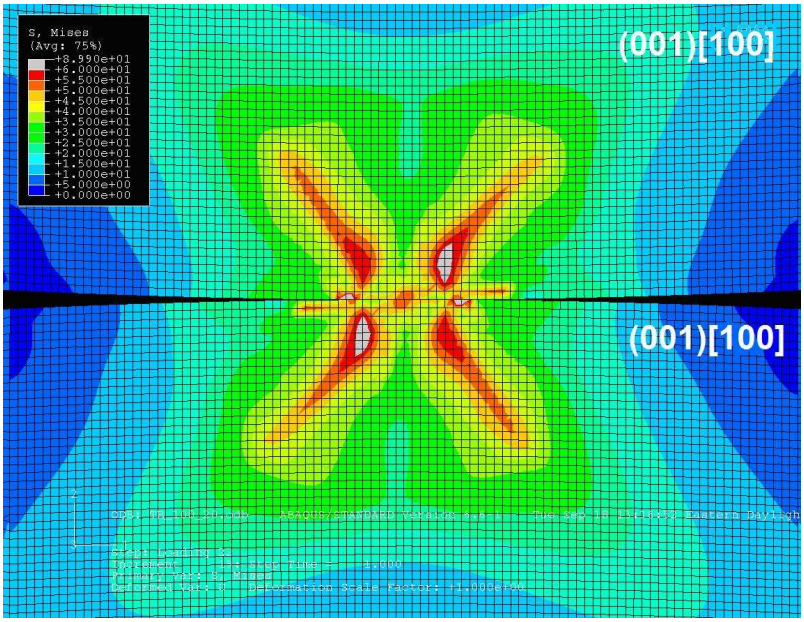

(a)

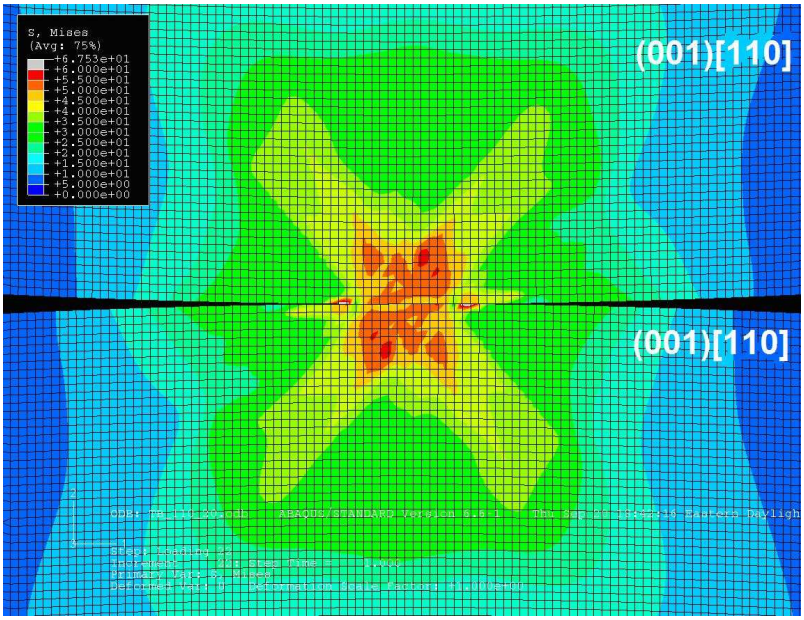

(b)

Figure 35: Von Mises Stress at maximum vertical interference (x/R =0) with ω*=20 for (a) (001)[100] over (001)[100] and (b) (001)[110] over (001)[110]

The results of the simulations run normal to the (110) plane translating in the $[001]$, $[\bar{1}11]$, and $[\bar{1}10]$ directions are unique from those run normal to the (001) cube face. The von Mises stress plots for these simulations on the (110) plane are shown in Figure 36. Translating in the $[001]$ direction an anti-symmetric 'X' pattern is seen with higher stress values in the direction of translation. Translating in the $[\bar{1}11]$ direction also demonstrates bands in intensified stress but they are in directions which are almost normal to the plane of contact. The higher stress values extend much further subsurface than in the other cases. This is as expected in light of the plastic strains discussed in the previous section. Translating in the $[\bar{1}10]$ direction shows similar features as in the other directions. The response is also very similar to the response of the simulation normal to the (001) plane translating in the $[110]$ direction, translating in an equivalent direction but different plane yields a similar stress response which may suggest the slip planes are being activated in a similar way. The results of the simulations normal to the (111) plane translating in the $[\bar{2}11]$, $[\bar{1}01]$, and $[\bar{1}\,\bar{1}2]$ directions are shown in Figure 37. There are more preferred directions on which the stress is intensified in these cases creating a star like pattern. Another key observation is that when sliding in the three different directions on the (111) plane there are no significant differences between the stress responses.

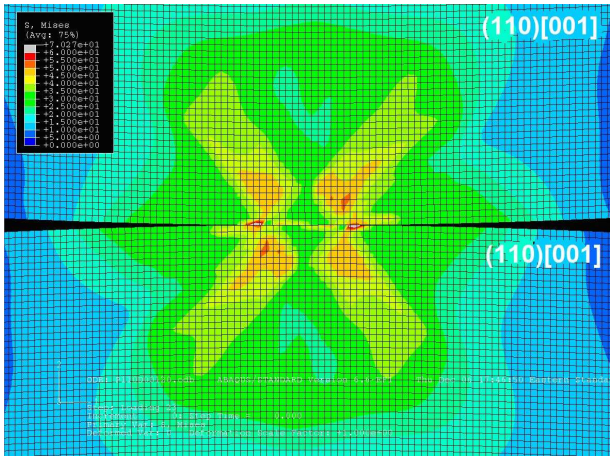

(a)

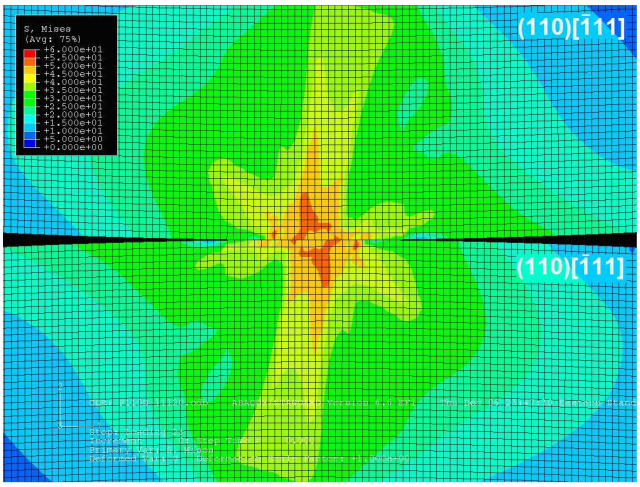

(b)

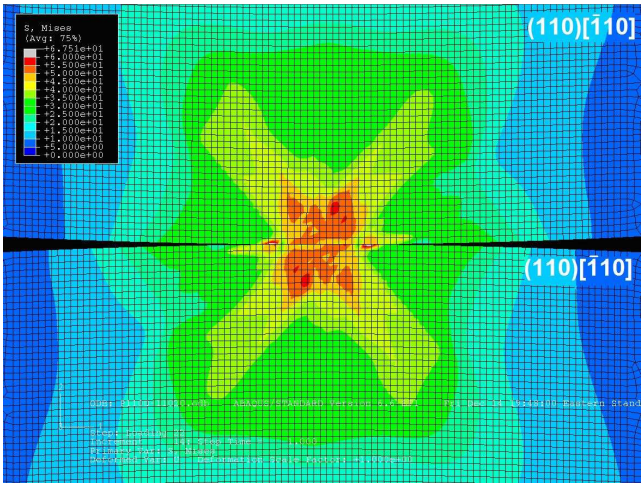

(c)

Figure 36: Von Mises stress at maximum vertical interference (x/R = 0) with $\omega^* = 20$ for (a) (110)[001] over (110)[001] (b) $(110)[\bar{1}11]$ over $(110)[\bar{1}11]$ (c) $(110)[\bar{1}10]$ over $(110)[\bar{1}10]$.

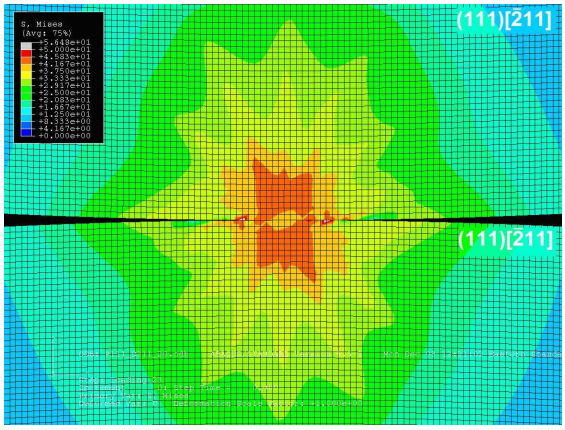

(a)

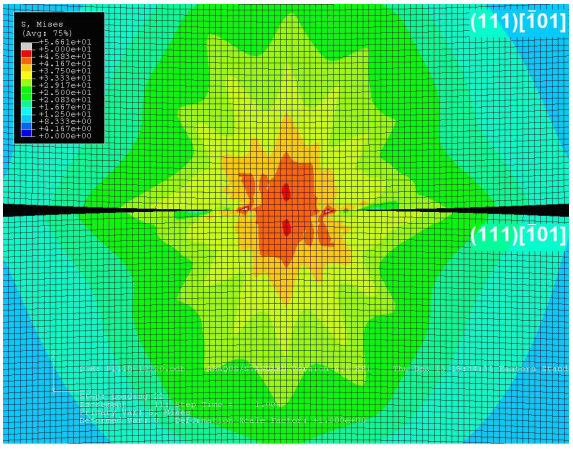

(b)

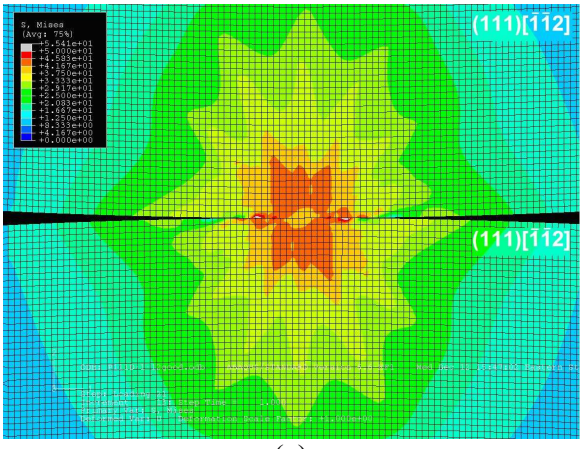

(c)

Figure 37: Von Mises stress at maximum vertical interference (x/R = 0) with $\omega^* = 20$ for (a) (111)[$\bar{2}$11] over (111)[$\bar{2}$11] (b) (111)[$\bar{1}$01] over (111)[$\bar{1}$01] (c) (111)[$\bar{1}\,\bar{1}$2] over (111)[$\bar{1}\,\bar{1}$2]

5.1.2 Residual Stress

Similar trends can be seen in the residual stress fields between the J_2 and crystal plasticity simulations, yet there are still differences between the simulations. The overall shape of the residual stress fields is the same but the plots for the crystal plasticity have a much less smooth appearance. Each residual stress plot has a pocket of zero stress beneath the surface along the x=0 axis, but the size and shape of this pocket varies based on the orientation. All of the residual stress plots are anti-symmetric about the vertical axis like the maximum interference stress plots. In general less residual stress in the asperity indicates more inelastic deformation has occurred this is demonstrated in Figure 39. The residual stresses are lower when normal to the (001) plane is translating in the [110] direction than when translating in the [100] direction. Simulations showing residual stress for the (110) plane is shown in Figure 40. When translating in the $[\bar{1}11]$ direction, shown in Figure 40(b), the residual stresses remain much deeper subsurface than when translating in the $[001]$ direction (Figure 40(a)) or $[\bar{1}10]$ direction (Figure 40(c)). Since the (110) $[\bar{1}11]$ is oriented such that the stresses are much deeper subsurface, more deformation occurs at that depth leaving a deeper residual stress field. The residual stresses in the simulations normal to the (111) plane shown in Figure 41 predict the same response for translating in all three directions. The subtle differences seen at the max loading step are no longer seen.

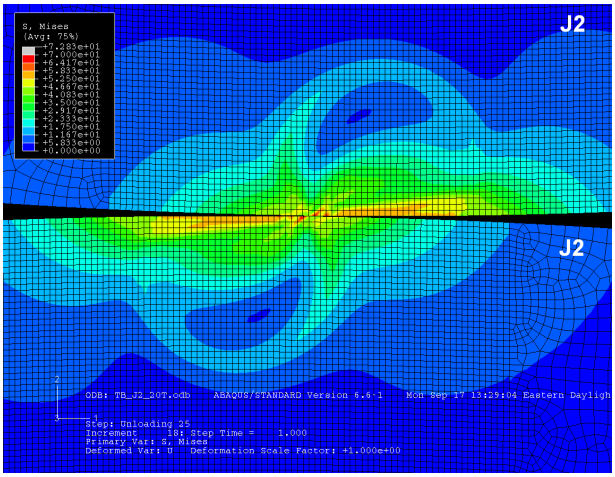

Figure 38: Von Mises stress after translating with $\omega^* = 20$ for isotropic over isotropic.

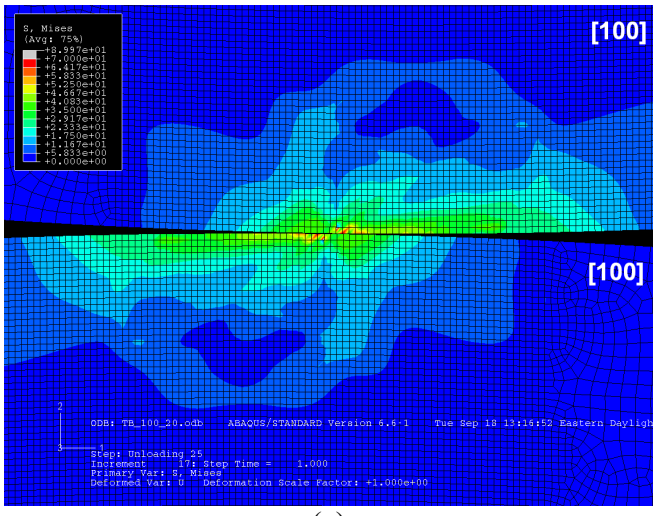

(a)

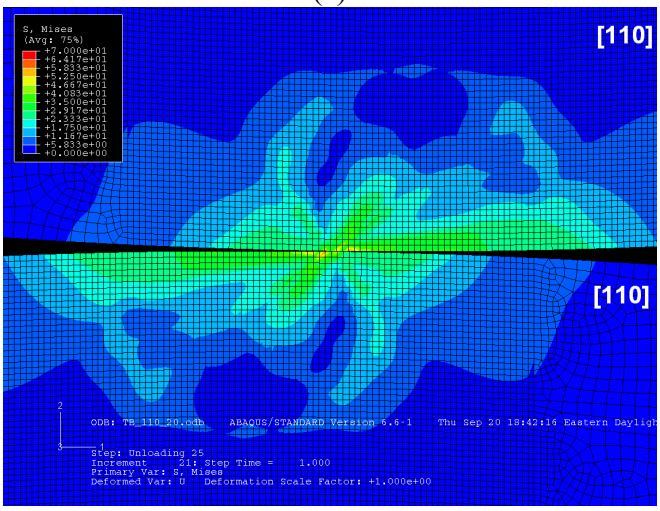

(b)

Figure 39: Von Mises stress after translating with $\omega^* = 20$ for (a) (001)[100] over (001)[100] (b) (001)[110] over (001)[110].

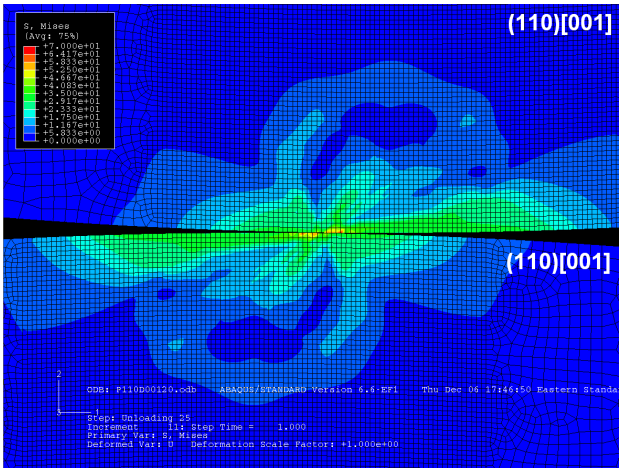

(a)

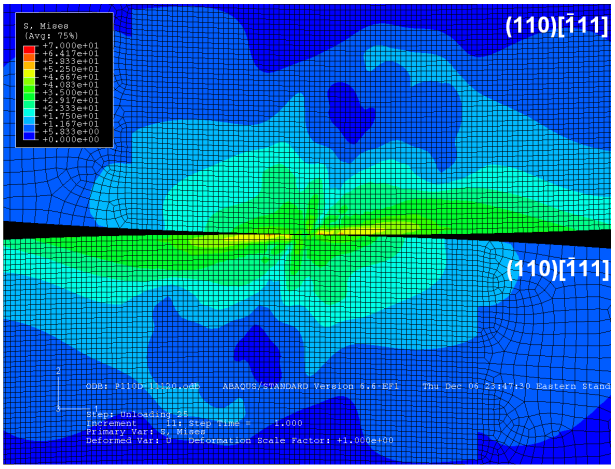

(b)

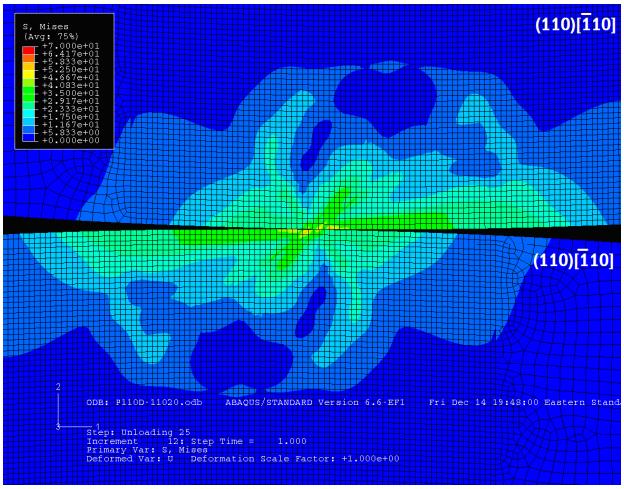

(c)

Figure 40: Von Mises stress after translating with $\omega^* = 20$ for (a) (110)[001] over (110)[001] (b) (110)[$\bar{1}$11] over (110)[$\bar{1}$11] (c) (110)[$\bar{1}$10] over (110)[$\bar{1}$10].

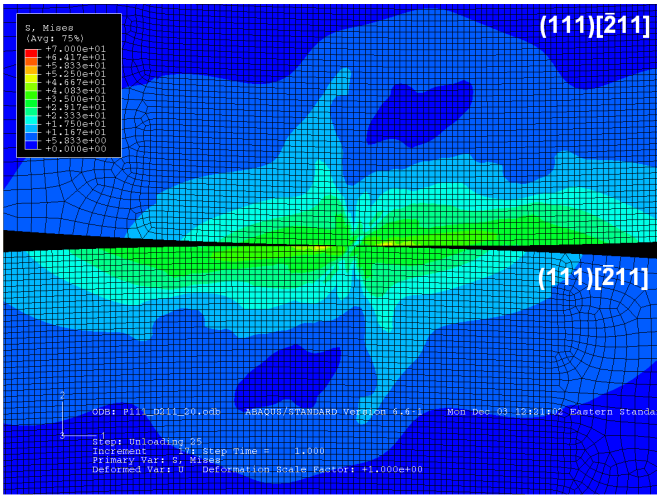

(a)

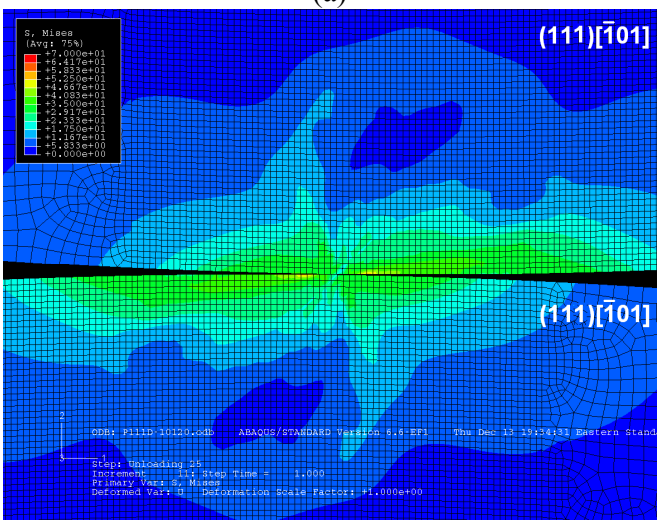

(b)

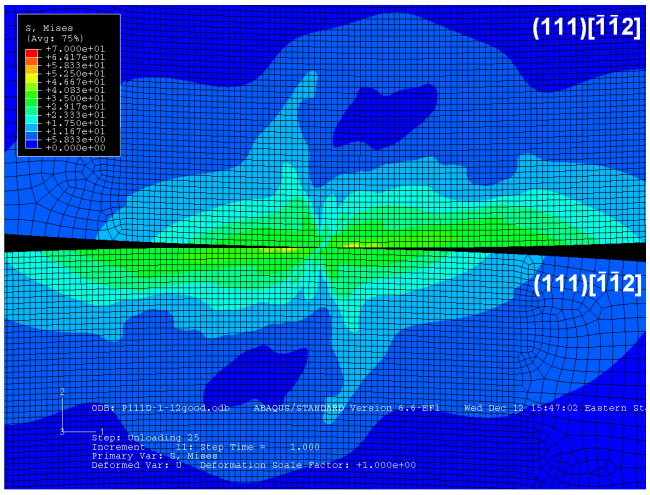

(c)

Figure 41: Von Mises stress after translating with $\omega* = 20$ for (a) $(111)[\bar{2}11]$ over $(111)[\bar{2}11]$ (b) $(111)[\bar{1}01]$ over $(111)[\bar{1}01]$ (c) $(111)[\bar{1}\,\bar{1}2]$ over $(111)[\bar{1}\,\bar{1}2]$.

5.3 Surface Deformations

The maximum vertical displacements at the surface during the translation are shown in Figure 42. Here, the maximum vertical displacement u_y of the surface nodes of the lower cylinder, normalized by the critical interference ω_c, is shown as a function of the normalized relative position x/R of the cylinders. Since plastic deformation occurs, there is residual displacement when the cylinders come out of contact at x/R = 0.28. When the interface is normal to the (001) plane and translating in the ⟨110⟩ direction, the magnitude of the maximum deformation at the surface is greater than when translating in the ⟨100⟩ direction. Hence, the residual deformation is higher when translating in the ⟨110⟩ direction, implying more flattening is experienced by the cylinders in this orientation. This is consistent with the larger effective plastic strain in this case. Interestingly, the J_2 plasticity case lies between these two crystal plasticity cases, which might be expected if J_2 plasticity represents an average response of the deformation of multiple crystals. Figure 42(b) shows the simulations with the interface normal to the (110) and (111) planes. Only one of the three simulations on the (111) plane was plotted because the results were identical for all three cases. The maximum surface deformation for all of the simulations on these two planes is similar.

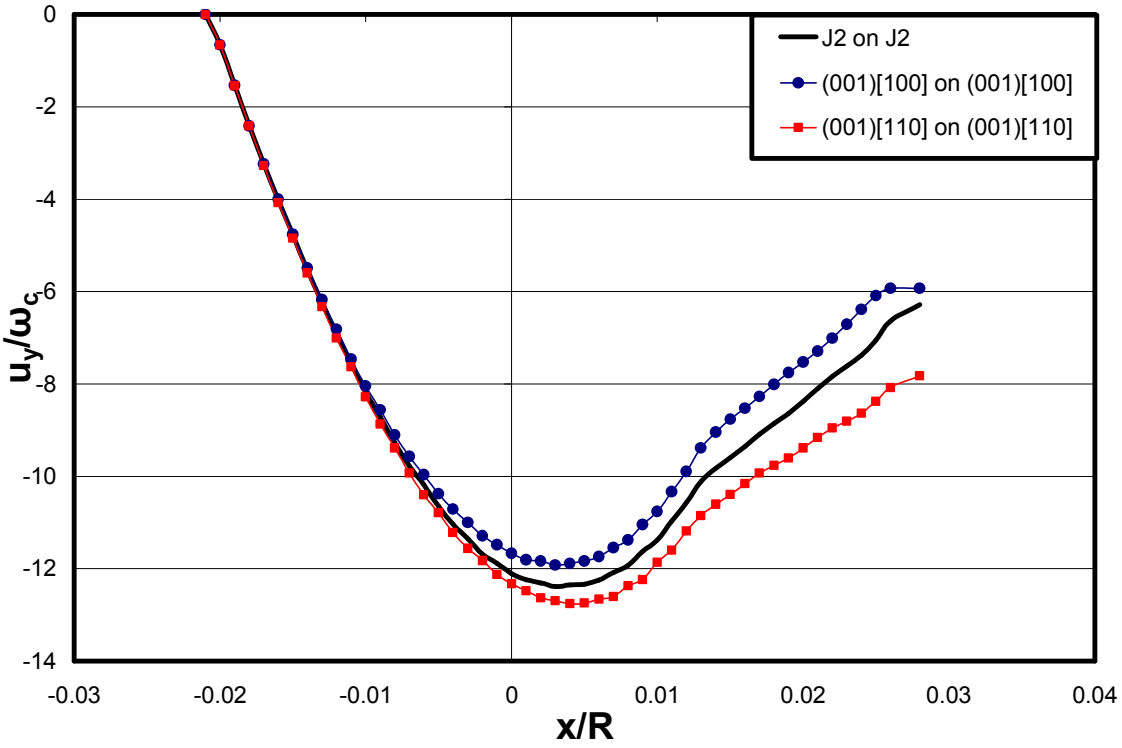

(a)

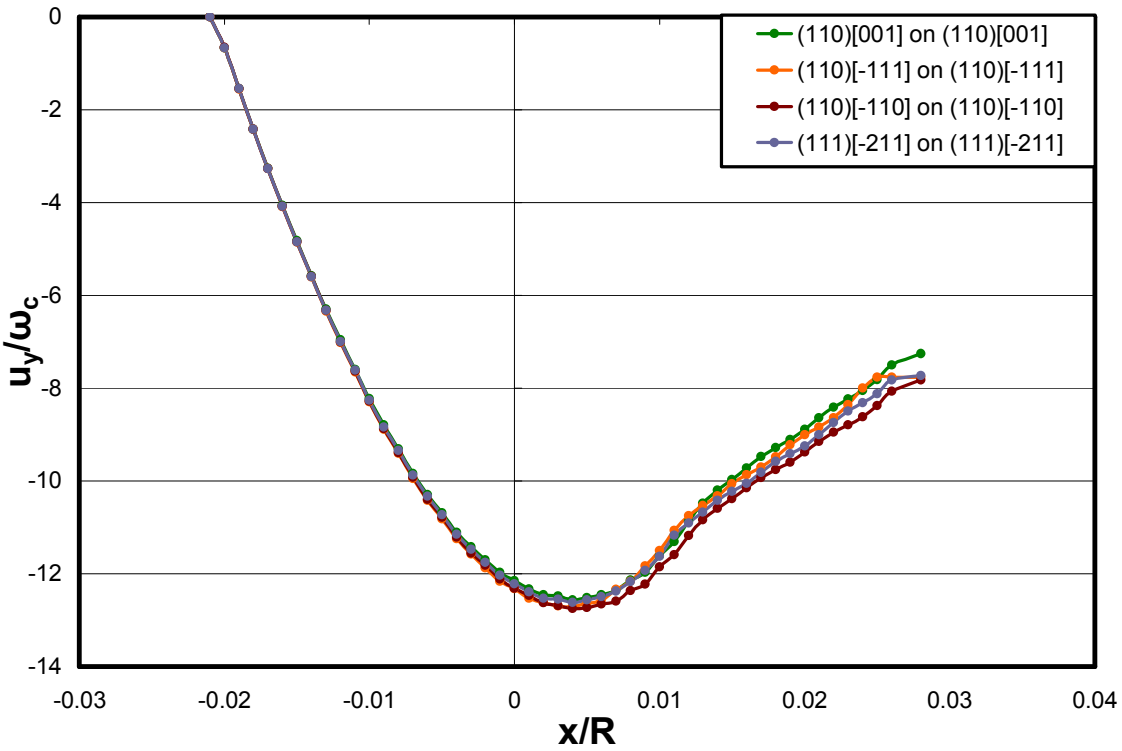

(b)

Figure 42: Maximum vertical surface displacement during translation for (a) isotropic and (001) plane (b) (110) and (111) planes.

5.4 Forces

5.4.1 Tangential

The summation of horizontal reaction forces at the base of the lower cylinder represents the magnitude of the tangential force during translation. This horizontal reaction force F_x, normalized by the critical load P_c as defined in the Chapter 4, is plotted as a function of normalized relative position in Figure 43. The horizontal reaction force initially increases compressively as the two cylinders come into contact and the interference increases. Plastic deformation occurs resulting in differences in the horizontal reaction force for the simulations of differently oriented cylinders. The peak compressive stress occurs before the cylinders are aligned. The tensile force near the end of the translation is the elastic spring back. When the deformation is completely elastic (i.e., when $\omega^* \leq 1$), the compressive reaction force is balanced by an elastic spring back force resulting in the horizontal reaction force path passing through the origin, x/R=0 [8]. Figure 43(a) shows that at the position of greatest resistance, $F_x/P_c = 0.082$ in the isotropic J_2 simulation compared to $F_x/P_c = 0.069$ in the crystal plasticity simulations. The difference between these values is related to the initial yield strength parameters in the two material models. If we compare the crystal plasticity simulations, we see that they follow an almost identical path upon loading, but the difference becomes evident after significant plastic deformation occurs. The difference between the two is quite notable when the cylinders are coming back out of contact ($x/R > 0$). On the (001) plane, the spring-back force for translation in the ⟨100⟩ direction is considerably higher indicating more elastic recovery than in the ⟨110⟩ direction. This is consistent with the height of the cylinder being reduced to a greater extent in the ⟨110⟩ direction due to

plastic deformation and hence there is a reduced amount of interference at the end of the translation in that case. The simulations run with the interface normal to the (110) and (111) planes, Figure 43(b) and (c), respectively, are similar, with the interface normal to the (111) plane, giving an identical response for sliding in all three directions.

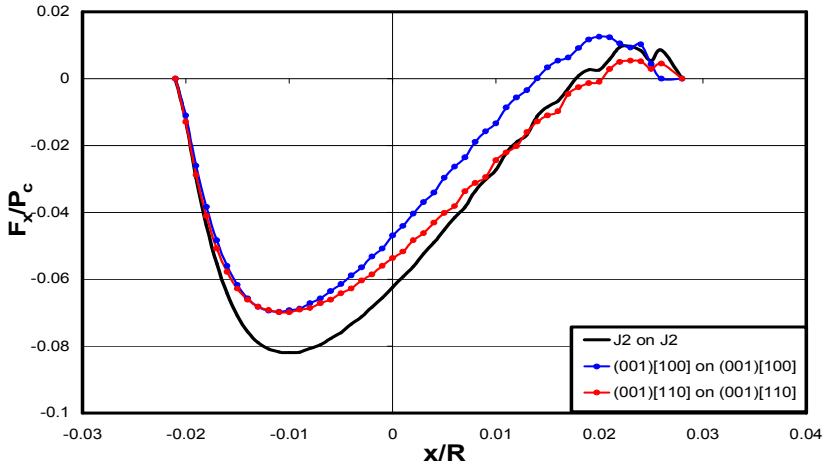

(a)

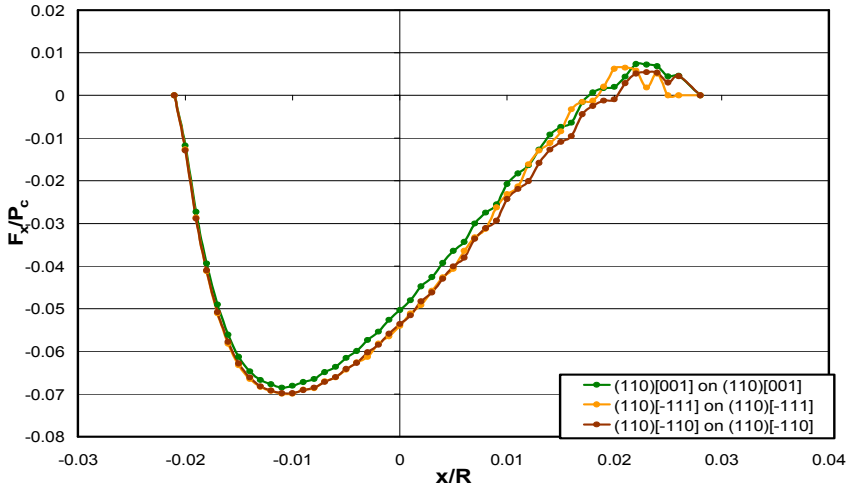

(b)

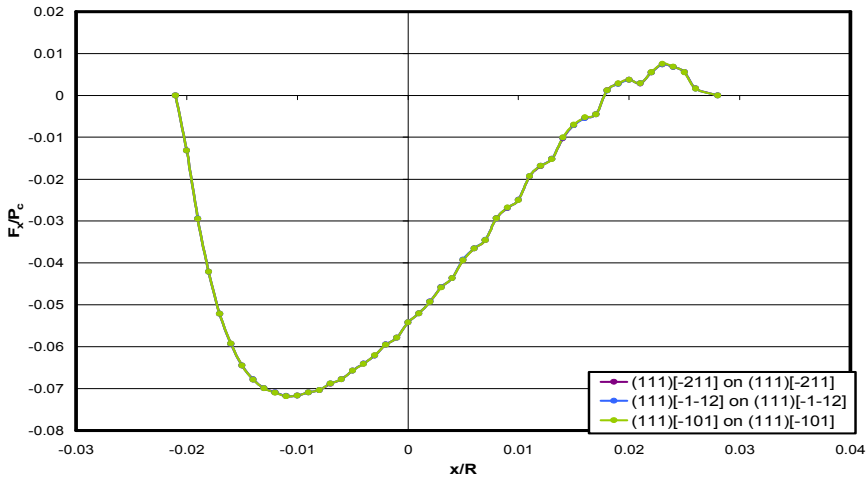

(c)

Figure 43: Tangential reaction force during translation for (a) isotropic and (001) (b) (110) (c) (111) plane simulations.

5.4.2 Normal Forces

The normalized normal force at the base of the cylinder during the translation is shown in Figure 44 for the various simulation cases. The maximum normal force occurs just before the cylinders are aligned. The normal force for the J_2 simulation is greater than that for the crystal plasticity simulations for the same reason that the maximum horizontal reaction force is greater. When on a (001) plane, translating in the ⟨100⟩ direction is the harder orientation, the normal force experienced for it is higher than that of the ⟨110⟩ orientation, $F_y/P_c = 13.39$ and 12.45, respectively. From Chapter 4 we found that under normal loading on the (001) plane the normal forces for the $(001)[100]$ and the $(001)[110]$ orientations are $F_y/P_c = 15.57$ and 14.92, respectively. The normal reaction forces for normal loading is higher than the normal reaction forces for sliding in all cases, and this trend is confirmed by all of the simulations run. Thus, more deformation occurs under sliding than at the same interference under normal loading.

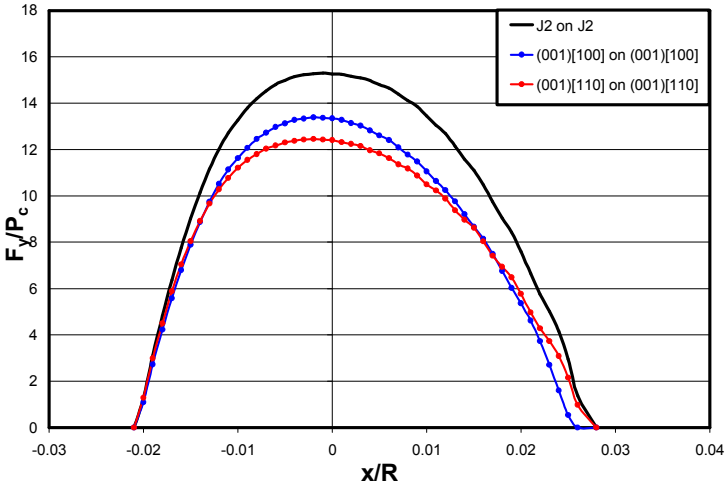

(a)

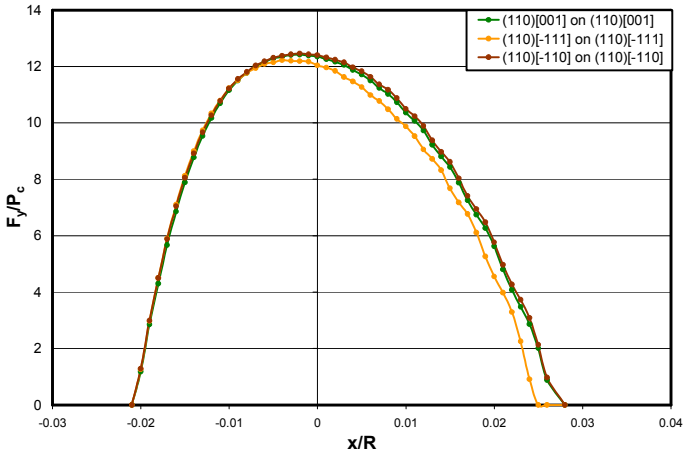

(b)

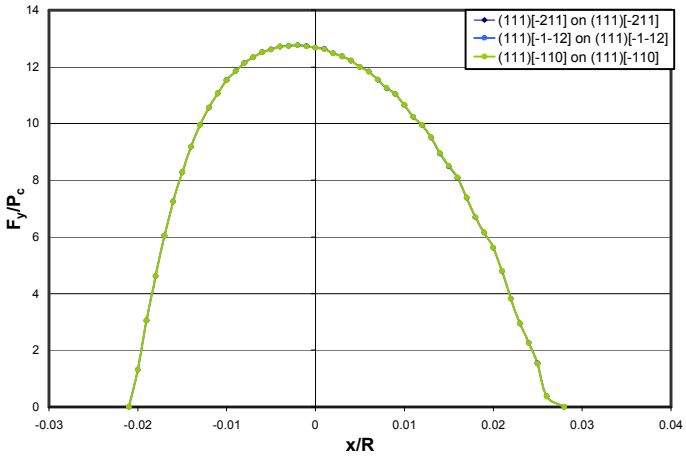

(c)

Figure 44: Normal force during translation for (a) isotropic and (001) (b) (110) (c) (111) plane simulations

5.5 Energy Dissipation

Using Eq. (2), the net energy dissipation, which is related to the plastic deformation component of COF, can be quantified by calculating the area under the horizontal reaction force vs. relative position curves shown in Figure 44. Since the cylinders do not displace in the normal direction, the normal force F_y does no work. The predicted energy dissipation for several combinations of faces and directions are summarized in Table 1. The energy dissipation is normalized by the critical energy U_c as defined by Green [28],

$$\frac{U_c}{L} = \frac{\pi (CS_y)^4 R^2}{4E'^3} \left\{ 4 \ln \left[\frac{2E'}{CS_y} \right] - 3 \right\}, \tag{17}$$

Where all parameters are as previously defined, and the critical energy U_c is defined per length L.

Table 2: Energy dissipation

Simulation	U_{net}/U_c	% Less energy dissipated than J_2
J2 on J2	1062.41	0.00
(110)[-110] on (110)[-110]	953.54	10.25
(001)[110] on (001)[110]	953.44	10.26
(111)[-211] on (111)[-211]	951.01	10.49
(111)[-101] on (111)[-101]	950.74	10.51
(111)[-1-12] on (111)[-1-12]	950.72	10.51
(110)[-111] on (110)[-111]	938.74	11.64
(110)[001] on (110)[001]	884.67	16.73
(001)[100] on (001)[100]	782.57	26.34

As discussed earlier, the COF is related to the energy dissipated, though a direct prediction of the COF using these energy dissipation results cannot be obtained because of the highly idealized asperity geometry and the assumption of zero adhesion. Because of the latter assumption, the predicted effective COF values are certainly much smaller

than experimentally measured values. But here, we isolate the component of friction due to plastic deformation, hence the results should still predict the correct trend in COF with crystal orientation when plastic dissipation is a significant component to friction. On the (001) face, sliding [100] on [100] dissipated the least energy. In fact, 21.8% more energy was dissipated when in the [110] on [110]. Conversely, the experimental study conducted by Bailey & Gwathmey [15] measured the COF on the (001) face to be approximately 50% (Figure 1(a)) higher when sliding in the [110] direction than when sliding in the [100] direction. It is clear that this trend has been captured, yet there are several more aspects that must be modeled to more closely capture the experimental values. Additional mechanisms of friction including adhesion and multiple asperity contacts coupled with more realistic asperity geometries would obviously be needed. Interestingly, translating on the (111) plane in any direction dissipates about the same amount as translating in the [110] direction on the (001) face. On the (110) plane, translating in the [001] direction dissipated less energy than translating in the $[\bar{1}10]$ direction. In contrast, the isotropic J_2 simulation predicts the largest dissipation. In all cases simulated, crystal plasticity has a lower net energy dissipation and hence predicts a lower COF than J_2 plasticity.

5.6 Dissimilar Crystals

One can also study the interaction of asperities having different crystal orientation. Here, the case of translating (001) cubic faces is examined, one oriented in the [100] direction and the other in the [110] direction. The effective plastic strain after completing the translation is shown in Figure 45. The dissipation energies fell between the values from the [100] on [100] and the [110] on [110] simulations, as one might expect, shown in Figure 46. Flipping the orientations of the cylinders gives the same result, except of course the top cylinder is the highly deformed one in that case. The dissipation energy of the flipped cylinders is also the same as shown in Figure 46. When comparing the residual plastic strains for the [100] on [110] case to the cases when the orientations are the same, it can be observed that more deformation occurs in the [110] oriented cylinder when it is translates over a [100] oriented cylinder than when it translate over another [110] oriented cylinder. The [110] is a softer orientation than the [100] and therefore undergoes more deformation during the translation. The additional deformation that occurs in the [110] is counteracted by less deformation in the [100] compared to when they translate upon like orientations.

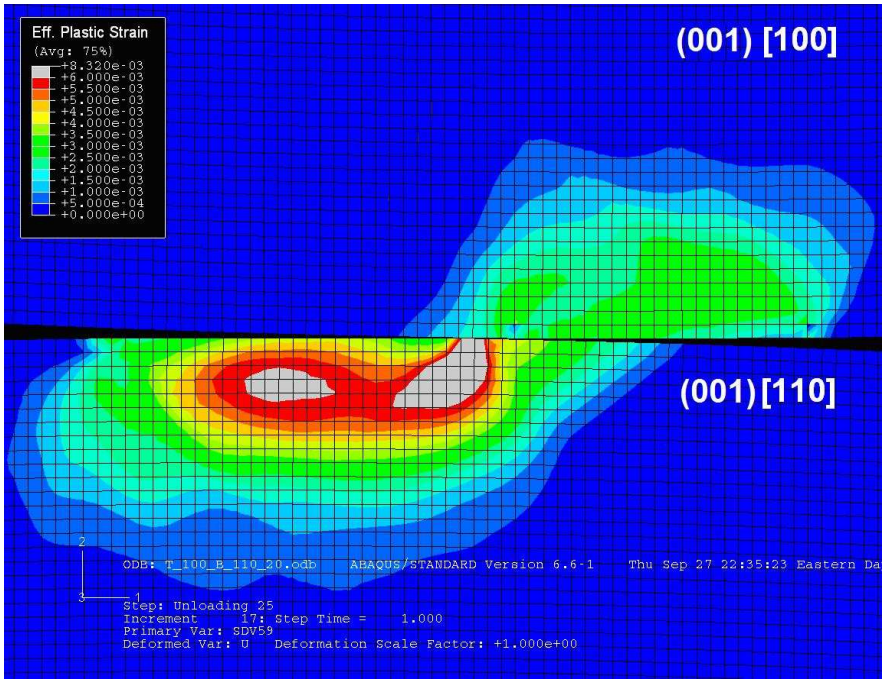

(a)

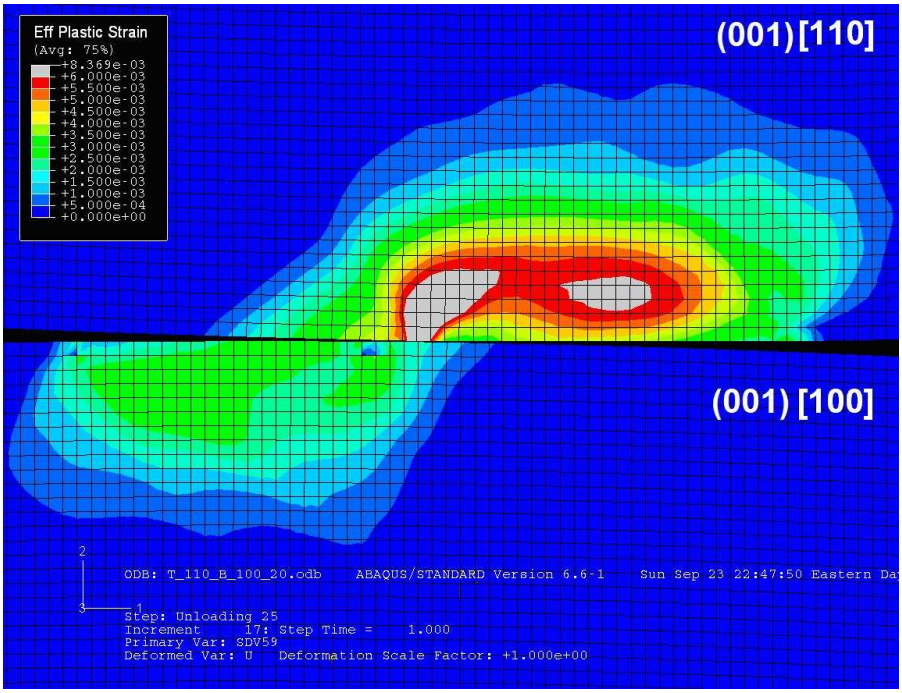

(b)

Figure 45: Effective plastic strain after translating cylinders with $\omega^* = 20$ for (a) (001)[100] over (001)[110] (b) (001)[110] over (001)[100]

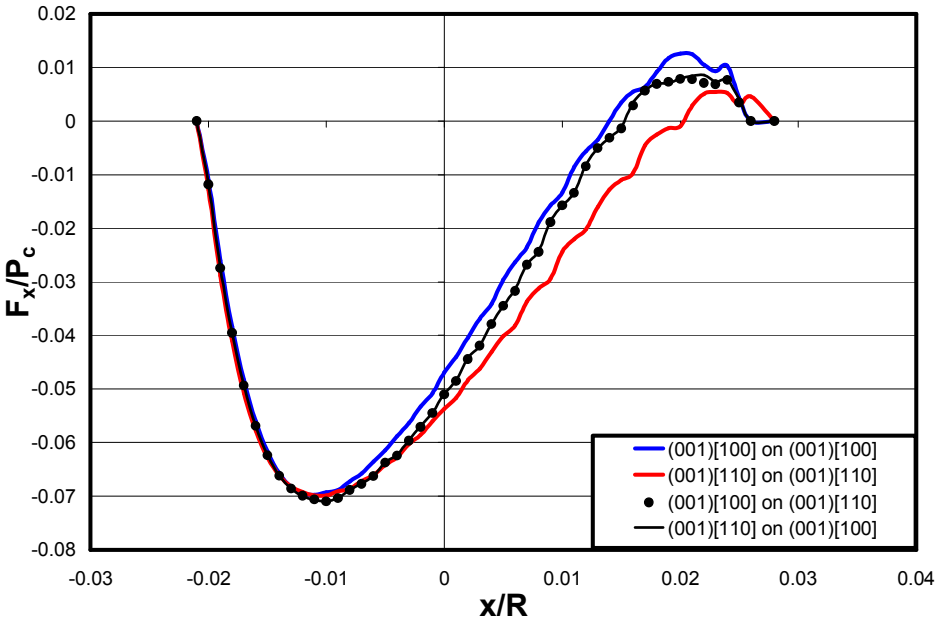

Figure 46: Horizontal reaction force during translation comparing different combinations of orientations.

CHAPTER 6: CONCLUSIONS

A modeling methodology has been proposed that is able to show clear differences in the response under normal and sliding contacts for different crystallographic orientations. Continuum crystal plasticity was used to capture these trends. There are key differences in the plastic strain and stress fields considering the size, shape, and magnitudes based on the orientation. Crystal plasticity is an effective method for representing the anisotropic nature of a single crystal material, and it can capture the asymmetries that will be present when the lattice is not symmetric relative to loading.

The results of this study were obtained running simulations on the specific planes and directions but the results for the families of those planes and directions can be generalized based on symmetry. It was found that the most significant anisotropies occurred under normal loading and sliding contact on the {001} planes. When the interface is normal to the {001} plane more energy is predicted to be dissipated when sliding in the ⟨110⟩ direction compared to sliding in the ⟨100⟩ direction. If the component of the COF associated with plastic deformation is significant, then the COF is higher in the case with greater energy dissipation. Therefore the total energy dissipated in the latter case is higher, indicating that the component of the COF associated with plastic deformation is greater leading to a higher measured COF.

The simulations conducted on the {111} plane did not show the anisotropies that were expected. The crystal plasticity model used does not account for latent hardening effects which cause hardening on a slip system based on the deformation on other slip systems. When sliding in the $\langle \bar{2}11 \rangle$, $\langle \bar{1}01 \rangle$, $\langle 2\bar{1}\bar{1} \rangle$, the anisotropies would be created

by the difference in the dislocation interactions based on the orientation. By not accounting for this effect in the crystal plasticity model the results of the simulations in the different orientations were the same. A future study should consider the effects of latent hardening on the response of the various simulations. In order to add latent hardening to the material model Eq. (4), which is the evolution equation for the drag strength, must be modified to,

$$\dot{g}^{(\alpha)} = 225\sum_{\beta=1}^{N_{sys}} q^{(\alpha\beta)} \left|\dot{\gamma}^{\beta}\right| - 2.05 g^{(\alpha)} \sum_{\beta=1}^{N_{sys}} \left|\dot{\gamma}^{\beta}\right| \tag{18}$$

where all parameters are as defined in Chapter 2, and $q^{(\alpha\beta)}$ is a ratio which relates the hardening of the drag stress on α slip system based on deformation on β slip system. It should be noted that the model would need to be recalibrated after making these changes using one of the previously mentioned methods.

In practice there are numerous effects such as, the effect of oxides, strain rate effects, dislocation densities and interaction, adhesive forces that make the interaction between asperities particularly difficult to model. So admittedly, this was a highly idealized study with some limitations that can likely be resolved with refined models, though with additional computational expense. But the main goal was to show that microstructural attributes such as crystallographic orientation, grain size and the like can be explicitly captured in contact mechanics modeling using continuum crystal plasticity material models. This is becoming increasingly important as the scale of the material and the contact become smaller such as in bridging the gap between molecular dynamic simulations and the macroscopic homogenous scale. In the future, one might consider imposing a very high COF at the interface to simulated localized welding which is the other extreme case of adhesion occurring after the asperities come into contact. It should

be noted that, several simulations were attempted imposing various high COF (1.0-1.5), but none of the FE simulations would converge with $\omega^*=20$.

REFERENCES

1. Jackson, R.L., and I. Green, A Finite Element Study of Hemispherical Contacts. in *Contact Mechanics - Friction: Modeling and Experiment*, (2003), 65-72. (ASME/STLE Tribology Conference)

2. Jackson, R.L., and I. Green, *A Finite Element Study of the Residual Stress and Deformation in Hemispherical Contacts*. *ASME Trans. Journal of Tribology*, 2005. **127**: 484-493.

3. Jackson, R.L., and I. Green, *A Finite Element Study of Elasto-plastic Hemispherical Contact Against a Rigid Flat*. *ASME Trans Journal of Tribology*, 2005. **127**: 343-354.

4. Kogut, L., and I. Etsion, *Elastic-Plastic Contact Analysis of a Sphere and a Rigid Flat*. *J. Appl. Mech*, 2002. **60**: 657-662.

5. Mesarovic, S.D., and N.A. Fleck, *Frictionless Indentation of Dissimilar Elastic-Plastic Spheres*. *Int. J. Solids Struct.*, 2000. **37**: 7071–7091.

6. Faulkner, A., and R.D. Arnell, *Development of a finite element model to simulate the sliding interaction between two, three-dimensional, elastoplastic, hemispherical asperities*. *Wear*, 2000. **242**: 114-123.

7. Moody, J., A Finite Element Analysis of Elastic-Plastic Sliding of Hemispherical Contacts *Mechanical Engineering*, Georgia Institute of Technology, Atlanta, GA, 2007, 103.

8. Vijaywargiya, R., and I. Green, *A Finite Element Study of the Deformations, Forces, Stress Formations, and Energy Losses in Sliding Cylindrical Contacts*. *International Journal of Non-Linear Mechanics*, 2007. **42**: 914-927.

9. Cha, P.-R., D.J. Srolovitz, and T.K. Vanderlick, *Molecular dynamics simulation of single asperity contact*. *Acta Materialia*, 2004. **52**: 3983–3996.

10. Rigney, D.A., and J.E. Hammerberg, *Unlubricated Sliding Behavior of Materials*. *MRS Bulletin*, 1998. **23**: 32-36.

11. Rigney, D.A., and J.E. Hammerberg, Mechanical mixing and the development of nanocrystalline material during the sliding of metals. in *The 1999 Julia R. Weertman Symposium on Advanced Materials for the 21st Century* (1999), 465-474.

12. Goh, C.H., D.L. McDowell, and R.W. Neu, *Plasticity in Polycrystalline Fretting Fatigue Contacts*. *Journal of the Mechanics and Physics of Solids*, 2006. **54**: 340-367.

13. Goh, C.H., D.L. McDowell, and R.W. Neu, *Influence of Microstructure in Partial-Slip Fretting Contacts Based on Two-Dimensional Crystal Plasticity Simulations*. *ASME Trans. Journal of Tribology*, 2006. **128**: 735-744.

14. Mayeur, J.R., D.L. McDowell, and R.W. Neu, *Crystal plasticity simulations of fretting of Ti-6Al-4V in partial slip regime considering effects of texture*. *Compuational Materials Science,* 2008. **41**: 356-365.

15. Bailey, J.M., and A.T. Gwathmey, *Friction and Surface Deformation During Sliding on Single Crystals of Copper*. *American Society of Lubrication Engineers-Trans.*, 1962. **5**: 45-56.

16. Ohmae, N., T. Tsukizoe, and F. Akiyama. On the Mircoscopic Processes Involved in Metallic Friction *Philosophical Magazine*, 1979, 803-810.

17. Buckley, D.H., *Surface Effects in Adhesion, Friction, Wear, and Lubrication*. 1981: Elsevier.

18. Lee, W.B., S. To, and C.F. Cheung, *Effect of Crystallographic Orientation in Diamond Turning of Copper Single Crystals*. *Scripta Materialia*, 2000. **42**: 937-945.

19. Kuhlmann-Wilsdorf, D., *Dislocation Concepts in Friction and Wear*. *Fundamentals of Friction and Wear of Materials, ed. D.A. Rigney (Metals Park, OH: American Society for Metals, 1981)*, 1981. 119-186.

20. Dyer, L.D., *The Actual Dislocation Distribution Around a Ball Indentation on the Cube Face of Copper*. *Trans. ASM*, 1965. **58**: 620-644.

21. Huang, X., T.E. Gibson, M. Zhang, and R.W. Neu, *Fretting Behavior of a Single-Crystal Ni-base Superalloy at Room Temperature*. *Tribology International, Submitted for Review*, 2007.

22. Casals, O., J. Ocenasek, and J. Alcala, *Crystal plasticity finite element simulations of pyramidal indentation in copper single crystals*. *Acta Materialia*, 2007. **55**: 55-78.

23. ABAQUS, Hibbitt, Karlsson, and Sorensen, Inc, Providence, RI, v 6.6.2006.:

24. Tanner, A.B., R.D. McGinty, and D.L. McDowell, *Modeling temperature and strain rate history effects in OFHC Cu*. *International Journal of Plasticity*, 1999. **15**: 575-603.

25. McGinty, R.D., and D.L. McDowell, *Multiscale Polycrytstal Plasticity*. *Journal of Engineering Materials and Technology*, 1999. **121**: 203-209.

26. Horstemeyer, M.F., D.L. McDowell, R.D. McGinty, *Design of Experiments for Constitutive Model Selection: Application to Polycrystalline Elastoviscoplasticity*. *Modeling and Simulation in Materials Science and Engineering*, 1999. **7**: 253-273.

27. Raabe, D., F. Roters, F. Barlat, and L.-Q. Chen, *Continuum Scale Simulation of Engineering Materials: Fundamentals-Microstructures- Process Applications*. 2004: Wiley-VCH.

28. Green, I., *Poisson Ratio Effects and Critical Values in Spherical and Cylindrical Hertzian Contacts*. *International Journal of Applied Mechanics*, 2005. **10**: 451-462.

29. Johnson, K.L., *Contact Mechanics*. 1985: Cambridge University Press.

30. Chen, W.T., *Stresses in Some Anisotropic Materials Due to Indentation and Sliding*. *International Journal of Solids and Structures*, 1969. **5**: 191-214.